Effect of Nitrogen Pressure on the Fabrication of $AlCrFeCoNiCu_{0.5}$ High Entropy Nitride Thin Films via Cathodic Arc Deposition

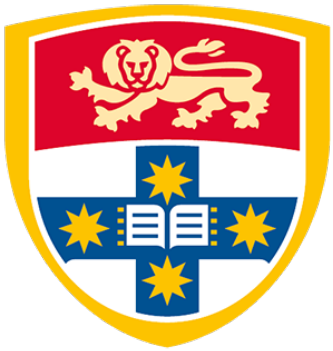

THE UNIVERSITY OF SYDNEY

Tenghao Jiang

A thesis submitted to fulfilment of the requirements for the degree of Master of Philosophy

School of Chemical and Biomolecular Engineering

University of Sydney

2023

Table of Content

Copyright Clearances

Statement of Originality

I hereby declare that the content presented in this thesis is the result of my own original research and represents my independent work. This thesis has not been submitted, in whole or in part, for the award of any other degree or qualification.

I further affirm that all sources utilised in the preparation of this thesis have been duly acknowledged, and any assistance received during its development has been appropriately recognised.

Printed name: Tenghao Jiang

Signature:

Date: 11 July 2023

Abstract

High entropy alloys (HEAs), consisting of five or more than five elements in equal or nearly equal proportions, usually exhibit superior mechanical properties, outstanding corrosion & oxidation resistance, and exceptionally high thermal stability compared to traditional alloys. HEA thin films possess further improved mechanical properties due to their nanocrystalline microstructure. Compared to HEA thin films, high entropy nitrides (HENs) have even higher mechanical strength and chemical inertness. $AlCrFeCoNiCu_{0.5}$ HEN thin film is reported to be an extraordinarily hard material that possesses high levels of surface protective nitrides layer, while limited work of $AlCrFeCoNiCu_{0.5}$ HEN thin film deposited by cathodic arc has been done. In this work, $AlCrFeCoNiCu_{0.5}$ HEN thin films were deposited on (100) Si wafer using a filtered cathodic arc. The nitrogen concentration for each thin film was regulated by changing pressure during depositions, tuning the distortion energy and mechanical properties. STEM-EDS revealed increased aluminium concentration as pressure increased. X-ray photoelectron spectra revealed that AlN was the preferred nitride formed. Interstitial solid solution of nitrogen enhanced the lattice distortion in the HEN films, while stronger covalent bonds contracted the crystal lattice according to XRD and HRTEM images. Amorphization was observed in the thin film with increased pressure. The mechanical properties of the cathodic arc deposited $AlCrFeCoNiCu_{0.5}$ HEN thin films were found to improve when pressure increased with the highest hardness of 12.4 □ 0.6 GPa and elastic modulus of 347.3 □ 17.7 GPa found at the highest pressure of 0.05 Pa. These mechanical properties were significantly enhanced compared to those of similar films fabricated by RF magnetron sputtering.

Acknowledgment

I would like to express my deepest gratitude to my esteemed supervisors, Professor Zongwen Liu and Professor Marcela Bilek, for their invaluable guidance and support throughout this research project. I extend my sincere appreciation to Dr Kostadinos Tsoutas for his equally dedicated supervision and valuable contributions to this research endeavour.

I would like to acknowledge the significant contributions of Dr Hong Zhao for his assistance with the nanoindentation experiments and insightful discussions, as well as the proof-reading and suggestion to my writing skills. Also, thanks to Dr Zhong Zheng for his expertise in TEM specimen preparation, TEM imaging, and valuable discussions. Additionally, I am grateful to my colleagues, Dr. Ian Falconer, Mr. Julian Whichello, Mr. Fanjun Xu and Mr. Joey Liang, for their collaborative efforts and support during this research project.

I would also like to extend my thanks to the staff of the University of Sydney Engineering Faculty, the University of Sydney HDR Group, Sydney Analytical (SA), Sydney Microscopy & Microanalysis (SMM), Research and Prototype Foundry (RPF), and Sydney Manufacturing Hub (SMH) for their support and assistance in providing the necessary resources and facilities for this research.

Furthermore, my heartfelt appreciation goes to my family, especially Ms Pei Lin and Mr Feng Jiang, for their unwavering financial and emotional support and my partner, Miss Jiawei Wu, for her constant support, assistance with daily challenges, and caring presence.

Lastly, I would like to acknowledge the Australia Chinese International Student Club (ACISC) and my many friends for their camaraderie and support.

Authorship attribution statement

This project has been accepted by the journal: “Journal of Vacuum Science & Technology A”. I designed the study, analysed the data and wrote the drafts of the manuscript.

In addition to the statements above, in cases where I am not the corresponding author of a published item, permission to include the published material has been granted by the corresponding author.

Printed name: Tenghao Jiang

Signature:

Date: 11 October 2023

As supervisor for the candidature upon which this thesis is based, I can confirm that the authorship attribution statements above are correct.

Printed name: Zongwen Liu

Signature:

Date: 12 October 2023

List of Figures

List of Tables

List of Acronyms

HEA – High Entropy Alloy

HEN – High Entropy Nitride

CAD – Cathodic Arc Deposition

XRD – X-ray Diffraction

XPS – X-ray Photoelectron Spectroscopy

AFM – Atomic Force Microscopy

TEM – Transmission Electronic Microscopy

FCC – Face-centred Cubic

BCC – Body-centred Cubic

RF – Radio Frequency

STEM – Scanning Transmission Electron Microscopy

EDS – Energy Dispersive X-ray Spectroscopy

HRTEM – High-resolution Transmission Electron Microscopy

FIB – Focus Ion Beam

3D – Three-dimensional

FFT – Fast Fourier Transformation

1. Introduction

High entropy alloys (HEAs), consisting of five or more than five elements in equal or nearly equal proportions [1], usually exhibit superior mechanical properties [2-4], outstanding corrosion and oxidation resistance, and exceptional high thermal stability [4]. On this basis, it has been brought to attention that HEA thin films exhibit improved mechanical properties due to their nanocrystalline microstructure [5]. Consequently, these films show great promise for offering surface protection in a range of applications, such as nuclear facility [6], aerospace [7] and biomedical devices [8].

In comparison to HEA thin films, high entropy nitrides (HENs) exhibit a higher mechanical strength and chemical stability [9, 10]. These HENs consist of strongly nitride-forming elements, e.g. Al or Cr, such as (FeCoNiCrCu$Al_{0.5}$)Nx [11], (CoCrCuFeNi)Nx [12] and AlCrMoNiTi [13], exhibiting greater improvement of mechanical properties than their HEA thin films. Magnetron sputtered AlCrFeCoNi$Cu_{0.5}$ HEN thin film was reported to be an extraordinarily hard material with high levels of surface protective nitrides layer. It was suggested as a protective coating for turbines, engine blades, and aircraft bodies, among other aerospace uses [10].

Various techniques could be applied to fabricate HEN thin films, such as laser cladding [14, 15], magnetron sputtering [16], and cathodic arc deposition (CAD) [17, 18]. Among various HEN thin film fabrication methods, cathodic arc deposition offers several advantages, such as high deposition rates [19], high plasma ionisation, and controllable ion kinetic energy [20], which can synthesise denser and more homogeneous as-deposited thin films [21].

As AlCrFeCoNi$Cu_{0.5}$ HEN thin films had only been fabricated using RF magnetron

sputtering system [10], in this study, CAD was applied to synthesise the $AlCrFeCoNiCu_{0.5}$ HEN thin films to further study the microstructure and mechanical properties at different deposition pressures ranging from 0.005 to 0.05 Pa. X-ray diffraction (XRD), X-ray photoelectron spectroscopy (XPS), Atomic force microscopy (AFM) and Transmission electronic microscopy (TEM) was performed to characterise $AlCrFeCoNiCu_{0.5}$ nitride thin films. Nanoindentation was performed to test the mechanical properties of the thin films. The evolution of thin film microstructure, chemical composition, surface chemistry and mechanical properties due to different nitrogen pressures were analysed.

2. Literature Review

2.1. Fundamentals of high entropy alloys

High entropy alloys (HEAs) have emerged as a novel class of materials that consist of multiple principal elements in nearly equal atomic ratios, which results in unique and exceptional properties. The concept of HEAs was first introduced by Yeh et al. (2004), who proposed that adding minor elements to a primary component could facilitate the formation of solid solution alloys that possess improved properties [1]

The discovery of HEAs has resulted in a new alloying method, combining high concentrations of multiple key elements, thereby resulting in complex and random solid solutions [22]. This approach is based on the theory that the high entropy of mixing of these alloys causes a more stable microstructure and improved properties. HEAs have demonstrated great potential in various applications due to their unique and outstanding properties, such as high strength, excellent corrosion resistance, and high-temperature stability [22]. Figure 1 sketched a schematic diagram of a conventional alloy and a 5-component high entropy alloy.

The properties of HEAs are influenced by four core effects: the high entropy effect, sluggish diffusion, lattice distortion and the cocktail effect [23]. The high entropy effect stems from the high mixing entropy of the constituent elements, which causes a high degree of disorder while enhancing solid solution strengthening. The lattice distortion effect results from the different atomic radii of constituent elements, which leads to a distorted crystal lattice and improves the mechanical properties. The sluggish diffusion effect is caused by the sluggish diffusion of atoms in the solid solution, which further enhances the mechanical properties of HEAs. Finally, the cocktail effect is due to the interactions between the constituent elements, which modifies the electronic structure [23].

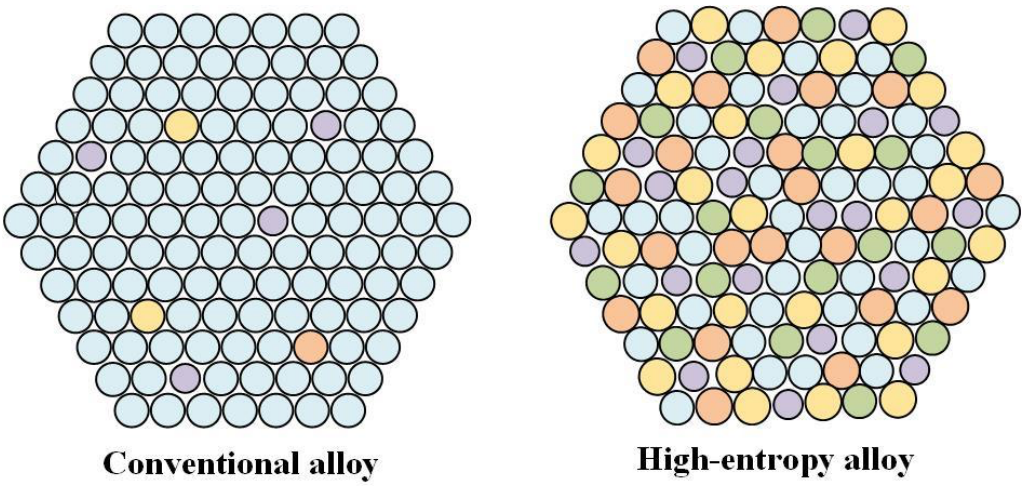

Figure 1. A schematic diagram of a conventional alloy (left) and a 5-component HEA (right) [23].

2.2. Four core effects of high entropy alloys

2.2.1. High entropy effect:

Entropy is a fundamental thermodynamic property that describes the degree of disorder or randomness in a system [24]. The entropy effect is recognised as a key factor in the design and development of novel materials with superior properties [1]. The concept of HEAs composed of multiple principal elements in equal or nearly equal atomic ratios

is based on the idea that high entropy of mixing results in a more stable microstructure and improved properties [23]. In recent years, HEAs have garnered a great deal of attention due to their unique and exceptional properties, and the high entropy effect plays a significant role in their formation and properties [25]. The high mixing entropy of the constituent elements in HEAs causes a high degree of disorder while enhancing solid solution strengthening, resulting in increased mechanical strength and hardness, improved thermal stability and enhanced corrosion resistance [26]. The high entropy effect is also the reason for the unique microstructure of HEAs that consists of complex and random solid solutions rather than simple intermetallic compounds [27].

However, the entropy effect is not limited to HEAs and applies to other materials, such as metallic glasses, polymers and ceramics [28]. In metallic glasses, it has been found that the entropy of mixing plays a crucial role in determining the glass-forming ability and mechanical properties [29]. In ceramics, the entropy effect causes the formation of solid solutions, leading to improved mechanical and thermal properties [30].

Experimental methods, for example, X-ray diffraction (XRD), transmission electron microscopy (TEM), and calorimetry (e.g. differential scanning calorimetry), have been used for investigating the entropy effect in materials [23]. These methods can study material microstructure, identify solid solutions formation, and measure alloys' formation enthalpy and entropy [23]. Thermodynamic modelling and simulation, such as Monte Carlo simulations, can also be used to investigate the entropy effect and predict the properties of materials [31].

Due to the high configurational entropy of mixing, the high-entropy effect decreases the solid solution phase's free energy. The greatest $R(ln(n))$ value in an equimolar mixture refers to the configurational entropy of mixing, where n is the number of

components and R is the gas constant [23]. When components are combined in equimolar amounts, the configurational entropy of the mixture is high, which favours and stabilises random solid solution phases at elevated temperatures. In addition, as the temperature increases, the solubility of the components in one another also increases, which reduces the number of phases in HEAs. This phenomenon can be seen in the XRD pattern of Figure 2, where a sequence of alloys that differ by one element from the previous alloy is shown.

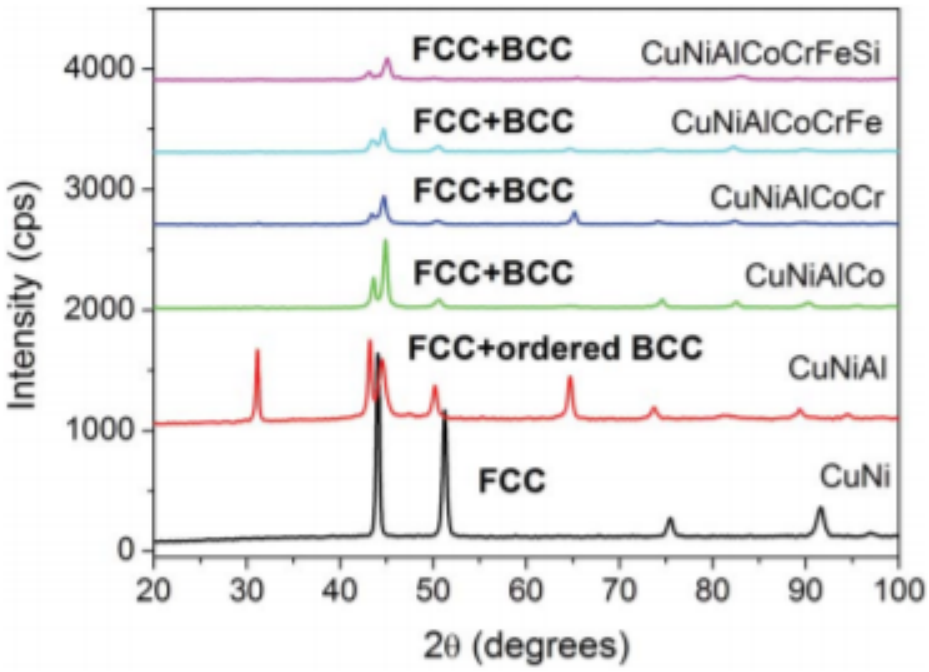

Figure 2. XRD pattern shows different crystal phases according to the change of major element number of alloys [22]

The XRD pattern of alloys with varying components demonstrates that adding more elements causes a simpler structure, resulting in face-centred cubic (FCC) and body-centred cubic (BCC) structures. A brief diagram of the FCC and BCC is shown in Figure 3. The high degree of disorder that results from the high mixing entropy of the constituent elements in HEAs improves solid solution strengthening, which results in increased mechanical strength and hardness, improved thermal stability and enhanced

corrosion resistance [32]. The entropy effect also contributes to the unique microstructure of HEAs, consisting of complex and random solid solutions rather than simple intermetallic compounds [23, 33].

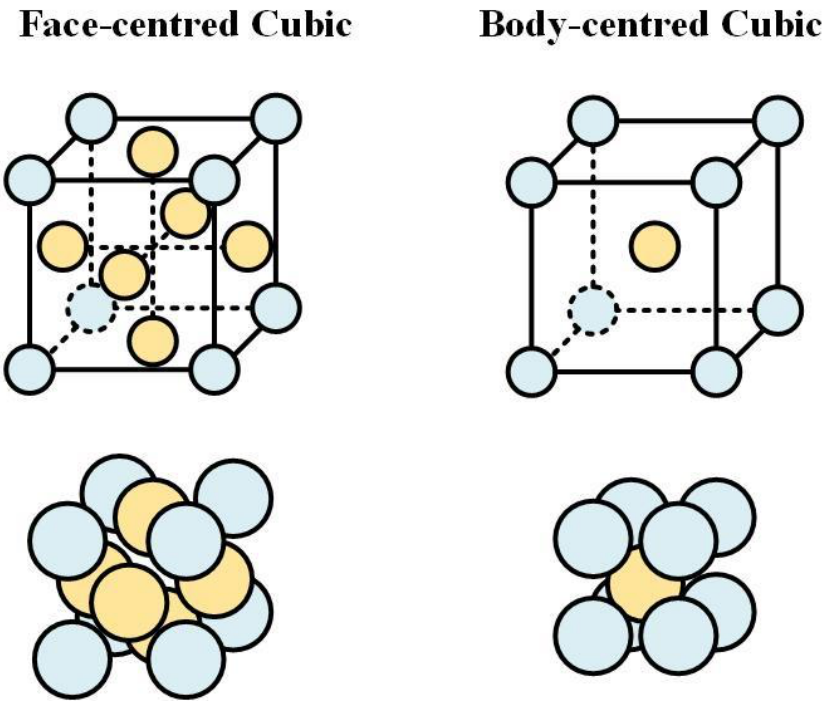

Figure 3. A schematic diagram of the FCC structure and BCC structure with atoms in different colours representing different elements [34]

2.2.2. Sluggish diffusion effect

The sluggish diffusion effect is a phenomenon that serves to describe how the diffusion kinetics in casted alloys are slower than those in ordinary alloys and pure metals. It was initially postulated as a means of explaining nano-precipitate formations in casted alloys such as AlCoCrCuFeNi due to diffusion rate limitations [1]. The deformed lattice of high entropy alloys slows atomic mobility, which leads to sluggish transport characteristics and nanometric-sized precipitate development due to lower nucleation and growth rates [1].

2.2.3. Lattice distortion

The lattice distortion effect is a key factor influencing HEA properties. A typical

schematic of five-component lattice distortion is sketched in Figure 4. The lattice distortion effect arises due to the size and electronegativity differences of the constituent elements, which leads to local lattice distortions and atomic-level strain fields in HEAs [35].

These lattice distortions significantly impact the mechanical, physical and chemical properties of HEAs. For instance, they can cause changes in the valence electron concentration and coordination of atoms, leading to variations in the density of states near the Fermi level and modifications to the electronic structure [36]. As a result, changes in the electrical and magnetic properties of HEAs can occur.

In addition, lattice distortion can enhance solid solution strengthening in HEAs. The atomic-level strain fields that arise from lattice distortions cause increased resistance to dislocation motion and deformation, which increases mechanical strength and hardness [35]. The lattice distortion effect also contributes to the enhanced thermal stability and corrosion resistance of HEAs as the strain fields inhibit atom diffusion, thereby preventing the formation of precipitates and corrosion products [36].

Experimental techniques, such as X-ray diffraction (XRD), transmission electron microscopy (TEM), and neutron diffraction, have been used to investigate the lattice distortion effect in HEAs [35]. These techniques can be used to determine HEA lattice parameters, atomic positions and bond lengths in addition to providing insight into the local lattice distortions and their impact on the properties of HEAs.

The lattice distortion effect is a critical factor influencing the mechanical, physical and chemical properties of high entropy alloys. Local lattice distortions and atomic-level strain fields that result from the size and electronegativity differences of the constituent elements enhance solid solution strengthening, which increases mechanical strength

and hardness, improves thermal stability, and enhances corrosion resistance.

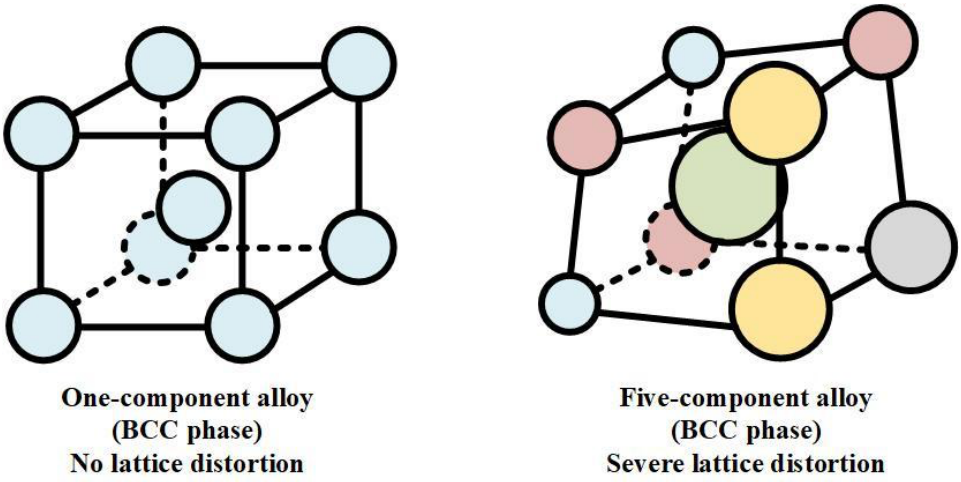

Figure 4. A schematic diagram showing the severe lattice distortion caused by different sizes of atoms in the crystal structure refers to the single BCC phase [37].

2.2.4. Cocktail effect

The cocktail effect is an intriguing and unique fundamental impact of high entropy alloys (HEAs). The cocktail effect in HEAs can be characterised as unexpected qualities resulting from synergistic effects that cannot be traced to any separate components. An example of a characteristic obtained from the law of mixing is the lattice parameter. However, the cocktail effect may also result in the improvement of wear resistance due to hard microstructure formation during precipitation. The composition and microstructure of HEAs significantly impact their characteristics [1]. Ranganathan was the first who proposed the idea of the cocktail effect, explaining the synthesis of HEAs by combining components in a "multi-metallic cocktail" [38]. According to Wang et al., the overall effect results from reciprocal interactions between constituent components, reducing excess amounts to the average levels indicated by the mixing rule [39]. Similarly, Yeh described the cocktail effect as an overall impact resulting from the composition, structure, and microstructure of HEAs [1].

2.3. Thin film

2.3.1. Fundamentals of thin film

The cost of HEA bulks is usually high as many of the compositions consist of rare metals. Therefore, HEA thin films began to be explored due to their lower cost. A layer of material with a thickness that ranges from one nanometre to several micrometres is defined as a film. The characteristics of HEAs that have been formed into thin films are different to those of bulk HEAs, which are closely related to various factors during film growth [21].

2.3.2. Film growth

The growth of film consists of four steps: condensation and nucleation, nuclear growth, interface creation and film growth [40]. Film density, surface area, shape and grain size are determined during these four steps. The surface chemistry, morphology and mechanical characteristics of the near-surface area of the film all influence the film process. [41]. Understanding the different film growth stages and the factors influencing them is essential to producing high-quality films with desired characteristics.

2.3.3. Condensation and nucleation

When atoms reach the substrate surface during the deposition process, they undergo collisions and reactions with the adsorbates, which leads to nuclei formation is referred to as the nucleation stage [21] and is influenced by various factors such as the mobility of atoms, location of nucleation, and nucleation density [42]. Atoms that do not immediately react with the surface of the substrate during the deposition process are known as adatoms, which have a certain amount of mobility on the surface before condensation occurs [43]. Adatom mobility is governed by their energy, and factors

such as low-energy ion bombardment can alter it [21]. The interaction of atoms with the surface also plays a crucial role in determining their mobility [21]. Furthermore, the surface free energy of different crystal surfaces can vary, and this can influence the adatom mobility and nuclei formation [21]. Nuclei size and distribution significantly impact the resulting film properties, such as thickness, texture, and grain size [42].

2.3.4. Nuclear growth

During the nucleation stage of film growth, adatoms lose energy and condense on the surface with other substrate atoms and chemical bonds are formed between them. The mobility of atoms determines the strength of the contact between them, with lesser mobility resulting in stronger contact. The surface atoms can be replaced with chemically absorbed atoms that form strong chemical bonds, which results in a "pseudomorphic" surface structure [42]. As the temperature increases, atom mobility on the surface of the substrate also increases.

Good nucleation locations are essential for better nucleation. Surface nucleus defects, including point defects and grain boundaries, foreign atoms embedded in the surface, surface patches with varying chemical or crystal orientations, and charge sites on the surface of insulators, are all examples of such locations [21]. Nucleation density is another important factor for determining nucleation quality and is defined as the number of nuclei per unit area. It must be high enough to generate a dense layer, cover the entire surface area with a thin film and make excellent contact with the surface [21].

The deposition rate also affects the nucleation density as adsorbed atoms on the moving surface may collide with other atoms on the moving surface or react with adsorbents on the surface, such as oxygen, to generate stable nuclei [21]. When an unstable surface is enriched with atoms, the surface characteristics may change. Various strategies for

changing the nucleation density can be adopted, including increasing the temperature and deposition rate, which enhance the likelihood of adatom collision. Surface chemistry can also be altered, making the surface more reactive or sensitising [42]. In addition, increasing nucleation density can be achieved by creating nucleation sites on the surface, such as high-energy particle bombardment to induce lattice defects, ion incorporation injection, or chemical replacement. Substances are incorporated into the surface, and charge centres on the surface of insulators are bombarded with electrons. A basecoat can also provide a superior surface for depositing required components [42].

2.3.5. Interface formation

With thin film formation, the interfacial zone between the film and substrate plays a vital role in determining the properties of the resulting film [21]. Several types of interfacial regions can form during film growth, including the abrupt interface, diffusion interface, compound interface, and pseudo-diffusion interface [44].

The abrupt interface is characterised by a sudden change to the material properties at the interface between the film and substrate, which can occur when the chemical bond between the deposited atoms and the substrate is weak, if there is a low deposition temperature, or if the substrate surface is contaminated [45]. This type of interface can result in interfacial voids as a result of low nucleation density and has poor adhesion due to facile fracture routes that develop through the gaps [21].

At the same time, the diffusion interface is formed by a gradual shift in composition across the contact area, which occurs without compound formation [46]. This interface type is generally observed when the film and substrate materials are in a solid solution with each other, and the temperature and timing are conducive to diffusion. The Kirkendall effect is first presented in the diffusion interface, which refers to the motion

of the interface between two metals that are caused by differences in metal atom diffusion rates [47]. However, this interface type can result in porosity, which leads to poor adhesion.

The compound interface is generated by the chemical reaction between the film and substrate materials, which creates a new phase at the interface. This type of interface is often brittle due to the volume changes that occur during the formation of new phases, which can cause microcracks, porosity and brittle compounds, ultimately resulting in poor adhesion [21].

Finally, the pseudo-diffusion interface is a graded composition and graded property interface that occurs when the deposition is graded from one material to the next. This interface type only occurs between insoluble materials at low temperatures; the phases are not generally separate [21].

Substrate surface cleaning and surface preparation techniques can be employed as a means of modifying the interface composition, structure and thickness. Contaminants that are weakly bound, such as water, carbon monoxide and hydrogen, can be removed from the deposition surface during the process, while highly bound pollutants, for example, oxygen, carbon and nitrogen, can drastically alter the interface response [48]. Other techniques can also modify the interface properties, such as adjusting substrate temperature, infusing energy into the surface area during deposition, or using concurrent ion bombardment or deposition of energetic particles [48].

Epitaxy between the substrate and the film is essential for achieving high-quality films. Epitaxial films have a highly ordered atomic arrangement following that of their substrates, which results in a homogeneous quality. The seed crystal or epitaxial film is a thin film that exhibits this highly ordered structure [21].

2.3.6. Film growth

Film growth is a complex process involving several crucial elements. One important factor that should be considered is surface roughness, which typically increases during film expansion. However, roughness can vary locally due to scratches, holes, embedded particles and particle contamination, which can cause changes in the film's characteristics [21]. Another important factor is adatom surface mobility. This factor is affected by surface temperature, absorbed gaseous compounds, and high-energy particle bombardment [49].

The incidence angle of the adsorbed atom flux also plays a crucial role in the columnar development of the film, as the geometric shadowing effect can cause the column to grow towards adsorbed atoms sources rather than perpendicularly to the surface [50]. In addition, the special substrate surface morphology can impact film production by affecting the ability of the deposition process to completely cover the surface without leaving exposed patches or pinholes [21].

Film density is another essential property that influences a variety of qualities, such as corrosion resistance, hardness, electrical resistivity, and index of refraction [51]. The deposition rate and incidence angle of the deposited particles can affect film density, columnar microstructure, and film performance during the bombardment, recoil implantation, sputtering, and redeposition [21].

Residual stress in atomic deposition films is common and can be either tensile or compressed. This stress can result in wrinkle spots with contamination and wavy patterns with a clean surface in compressed films and microcracks in tensile films [52]. The lattice strain associated with residual film stress can have various effects, including reducing recrystallisation temperature and enhancing mass transfer effects [21].

The gas incorporation portion is the final step of the film development process. A small percentage of gas may be introduced into the near-surface area as the surface is bombarded with gaseous ions. However, as the film grows, fresh film materials will continually cover the surface, causing the film to absorb the gas [21].

2.4. Thin film fabrication methods

Several different processes may be used for creating HEA thin films, such as laser cladding [14, 15], magnetron sputtering [7, 53], and cathodic arc deposition [17, 18].

2.4.1. Laser cladding

Laser cladding is a process that utilises a high-power laser to melt and fuse a powdered material onto a substrate. It can be employed to fabricate thicker HEA thin films of approximately 1-5 mm, making them significantly thicker than those produced by magnetron sputtering. For example, some high entropy alloys and nitrides were successfully fabricated using the laser cladding method, exhibiting superior mechanical properties and good chemical properties [54-56]. However, this method has drawbacks, such as incorporating substrate material into the film when using substrates with low melting temperatures and the possibility of surface irregularities, which can cause various defects [57, 58]. A schematic diagram of a laser cladding system is presented in Figure 5. The process starts with the delivery of powders carried by argon gas to the laser cladding head and then further to the nozzle. Subsequently, the powders are applied directly under the high energy-density laser beam and melted to form a melt pool. As the laser beam moves forward, the materials solidify and adhere to the substrate surface, forming homogeneous thin films with good adhesion to the substrate [59].

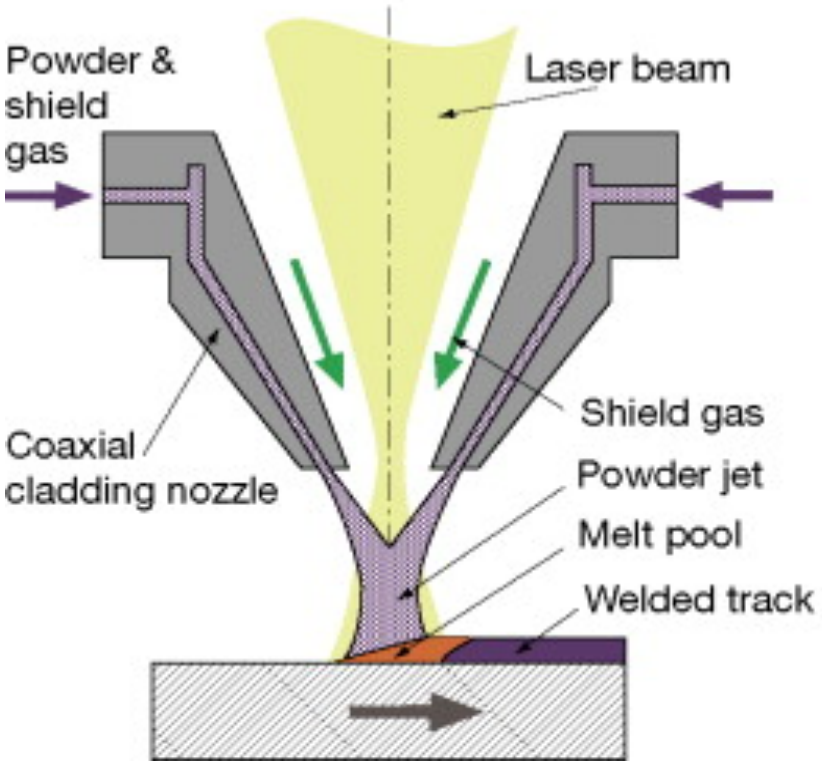

Figure 5. Schematic diagram of the laser cladding system [60].

2.4.2. Magnetron sputtering

Sputtering is a process usually used for depositing different coating materials on thin films, with a brief diagram of a magnetron sputtering shown in Figure 6. It can be employed in many applications, such as semiconductors, optical components, and photovoltaic solar cells. The technique uses the ejection of particles or ions with a wide energy distribution from the source onto the target or substrate [61]. The ions are ballistically expelled from the target land energetically on the substrate—the deposited materials on the substrate re-emit or re-sputter due to this [61].

The gas functions as a moderator at high pressures, colliding with the ions and diffusing them together to reach the substrates. Inert gases like argon are commonly employed as sputtering gases [62]. The atomic weights of the gas and target should be close to each other to facilitate efficient transfer. Neon is employed for light targets, while xenon or

krypton is used for heavier targets [62].

Unlike other deposition processes, sputter deposition can be utilised for materials with exceptionally high melting temperatures. It has also been discovered that the adhesion of sputtered films is greater than that of evaporated films [61]. The target can also contain many materials, which is useful for depositing many materials on surfaces. The sputter deposition target is incredibly convenient as it requires no maintenance [61]. Sputter deposition can also be used in ultra-high vacuum environments.

In addition, sputtering uses reactive gases (e.g., oxygen) and water-cooled materials to prevent materials from overheating. However, there are several significant drawbacks to sputtering methods, such as lift-off and contamination. Ion-assisted sputtering, high-target-utilisation sputtering, high-power impulse magnetron sputtering and gas flow sputtering are examples of sputter deposition processes [63].

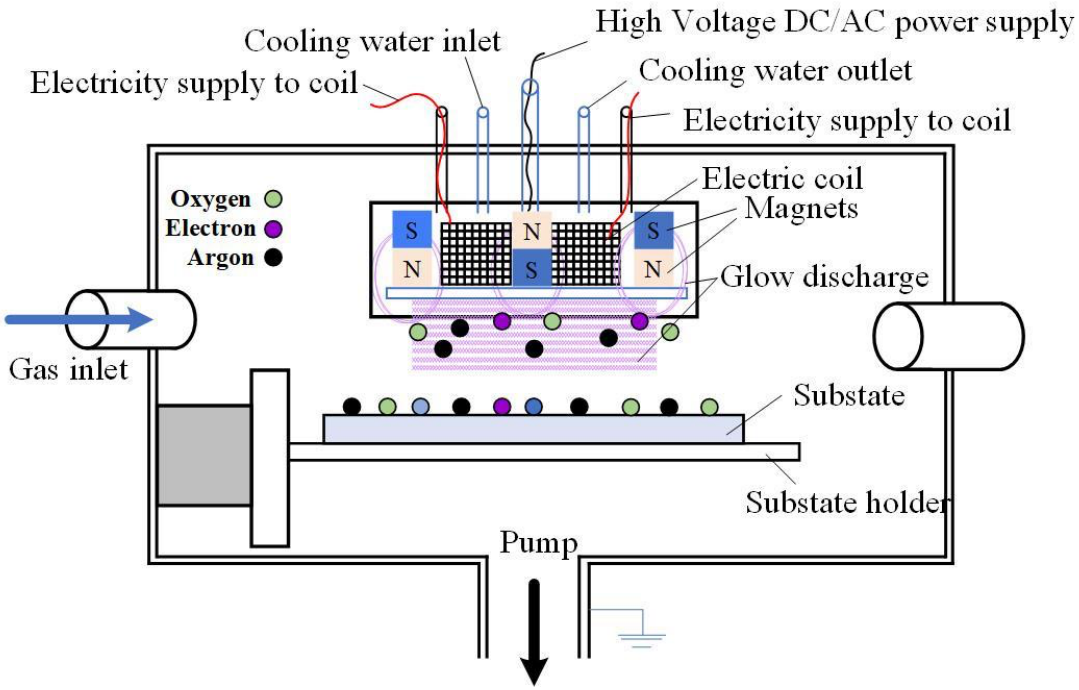

Figure 6. A brief diagram of the magnetron sputtering system [61].

The magnetic field is used in magnetron sputtering to configure charges (e.g., electrons) and plasma particles, as seen in Figure 6. When a magnetic field is utilised, an increase in collisions with inert gases close to the target surface will occur. With the utilisation of reactive, the sputtered atoms are subjected to chemical processes before they collide with the substrates. Chemical reactions occur when the sputtered atoms contact the reactive gases. Nitride and oxide films are created by reactive magnetron sputtering, and the element ratios can be adjusted using varied gas pressures [63].

2.4.3. Cathodic arc deposition

Cathodic arc deposition (CAD) was the fabrication method used for HEAs and HENs for this [61]. One commonly used structure of CAD machines is the half-circle channel. Two sets of arc source and anode are located on the two sides of the channel, while the substrate is placed in the centre. This option is often used to deposit films on both sides. In this project, the film was only deposited on one side of the substrate, and the major section that was used for one-side deposition of the CAD system is shown in Figure 7.

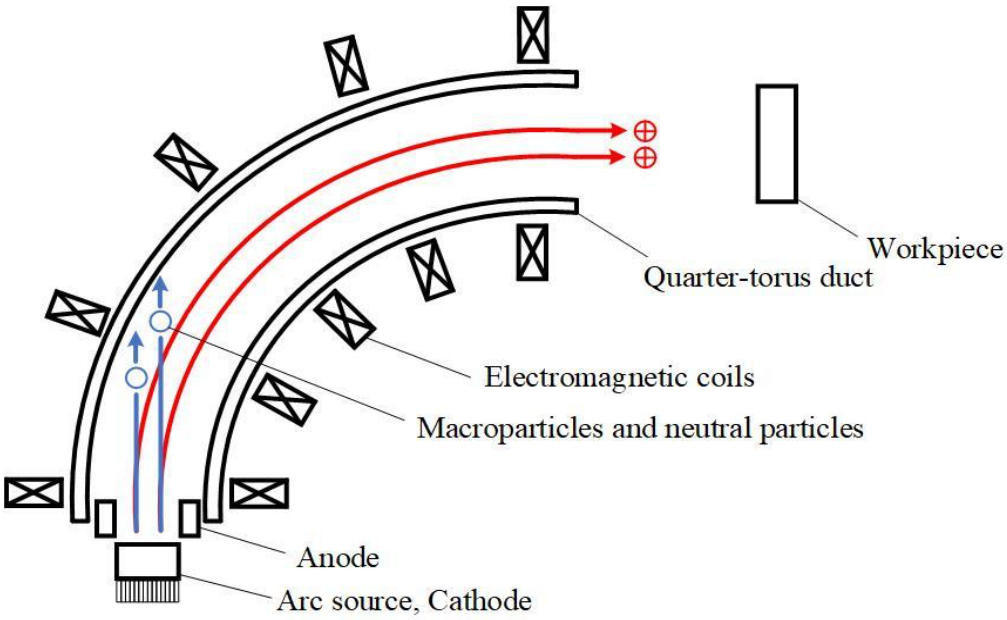

Figure 7. Diagram of the mechanism of the CAD with Aksenov quarter-torus duct macroparticle filter [20].

The arc source, also known as the cathode, was placed at one end of the channel and rounded by the anode. The workpiece, which will serve as the substrate, was positioned at the other end of the channel. The chamber is bent at 90 degrees with electromagnetic coils wound to guide the plasma towards the substrate and filter the microparticles [64].

CAD is a vapour deposition method that uses physical arcs. The solid cathode material is vaporised into an almost fully ionised particle by an electric arc. Arc evaporation occurs when strong current strikes, resulting in a micrometre-wide, incredibly energetic emission region called a cathode spot [48]. This cathode point is only active briefly before extinguishing and re-igniting in a new region near the previous crater, causing the arc to move.

A pure substance normally has three states: solid, liquid, and gas; however, the gas of the almost ionised particles discussed earlier is designated as the fourth state, called plasma [65]. The plasma pressure in the cathode point is high so that the plasmas will exit the surface [66].

Plasma emission is transforming an arc source into plasma and then emitting it. The four active phases of plasma emission are the pre-explosion stage, explosive emission stage, immediate post-explosion stage and final cool-down stage.

The local energy input at the cathode point is greater than that at neighbouring places during the pre-explosion period. Some favourable circumstances exist, such as a low local work function or an increased field caused by dielectric contamination and micro- or nano-protrusions [20]. With an incredibly strong electric field and high ion bombardment intensity, local energy input may produce electron emission with thermal runaway [20].

It then moves to the explosive emission stage, with a thermal runaway as its principal

characteristic [67, 68]. At this point, the micro-explosion destroys or erodes a microvolume, ultimately forming a minute crater on the cathode surface. It is worth mentioning that explosive occurrences occur in rapid succession.

The newly produced crater is extremely hot, and there is a strong likelihood that a surface layer of molten cathode is still present, and the surrounding plasma is quite dense. As a result, electron emission through field-enhanced thermionic emission remains high during the immediate post-explosion stage. Macroparticle formation induced by plasma pressure pressing on the liquid also occurs at this stage [69].

As thermal conduction increases the hot region and the temperature falls, electron emission ends exponentially in the final cool-down stage. The plasma that is generated explosively will be extended and its density reduced. Therefore, cathode sheath thickness increases and the electric surface field decreases. However, metal vapour may still escape from the heated surface, particularly if the cathode material has a high vapour pressure [48].

Intense emission can't be sustained in the plasma emission stages [48], which can be attributed to various factors. For example, heat conduction may expand the emission point size, causing the dissipated power to be dispersed over a broader area, and the density of the areal power will diminish over time. Another cause is the current being switched to a different route, as the portion of the cathode bulk just under the cathode spot has a higher resistance than the rest [48].

In addition, the emission centre constructs a resistive barrier to current flow, and as metal vapour is not a good conductor, it “chokes” the passage of electricity [48]. The emission area continues to expand as time passes (10s of nanoseconds) while the power density and corresponding local surface temperature drop, which results in the rapid

decline of electron emission.

The intense plasma at the emission point may trigger a fresh micro-explosion. The new facility and the previous, much bigger site are electrically connected. As less power is wasted there, the lower resistance channel takes over the current, accelerating the "death" of the initial emission location.

Mobility of the cathode spot is created by repeating the micro-explosion and extinguishing the micro-explosion at a different location with this method. The movement is largely random [48], and as a consequence, the probability of a new emission site igniting is isotopically distributed in the absence of an external magnetic field. A new emission site has the same likelihood of igniting in any direction from the current emission centre. The Random Walk model fairly approximates the real mobility of spots, despite the motion's apparent randomness [70].

At the same time, the random motion may be guided. Anything that can disturb the symmetry, such as a scratch on the cathode, surface pollution, contact with another material or an external magnetic field, can produce deviations from the random walk [48].

A quite significant particle mentioned in the previous section was macroparticles. When they develop, they are generally liquid, and as they move away from the cathode, they cool down and generate a defect when hitting a surface [71]. As a result, when thin films are deposited, the number of macroparticles on the film surface must be kept to a minimum. Macroparticle formation should be limited, and removing microparticles from plasma helps achieve this aim [72].

The arc current can be increased as a means of decreasing macroparticle formation. As boosting the arc current reduces the residence duration of the cathode spot, local heating

and evaporation are reduced [73]. In addition, it helps accelerate the deposition process [48]. The arc current is related to the rate of erosion on the cathode, and a continually increasing arc current results in uniform corrosion distribution on the surface of the cathode. If the arc current is too strong, the arc point may travel beyond the edge of the cathode, which will cause arcs on the material and release contaminating plasma or even result in the anode and chamber wall breaking down [73].

A filtering system is designed to separate the macroparticles. As has previously been stated, a chamber that is bent at 90 degrees is employed to filter macroparticles in the machine. The activated electromagnetic coils around the chamber will create a magnetic field to guide plasma flow towards the work item. Due to their huge size, these macroparticles are unaffected by electromagnetic fields [48]. Most particles will solidify and be reflected off the chamber wall. Producing structural faults in the coated film is still feasible due to this reflection. The bigger the charge-to-mass ratio in the particle, the easier it is to travel through the tube and onto the workpiece [48].

Therefore, changing the magnetic field will directly impact the filtering of macroparticles in the system. The magnetic field density and intensity increase when the current provided to the coils increases [71]. More ion collisions then occur, which results in charge transfer. The plasma can also be accelerated by a magnetic field, increasing the kinetic energy of the ions. However, with great magnetic field density, the magnetic mirror effect may occur, with particles approaching the substrate encountering increasing force and being reflected in the confinement area by the substrate [71].

Not only can the deposition process be concentrated on macro particle filtering, but it must also guarantee efficient plasma depositing. Two methods can be used to determine

plasma transport efficiency. The first is the ion number exiting the filter divided by the number of ions entering it, and when this ratio surpasses 25%, transportation is deemed efficient. The ion current ratio to the arc discharge current of the filtered plasma is an approach that is more usually utilised. The quantity of plasma that is produced roughly scales with the arc current. Transportation may be termed efficient With a ratio of 1 to 4 per cent [48].

$$\eta_{system} = \frac{I_{i,filtered}}{I_{arc}}$$

The energetic deposition is a process where most film-forming ions or atoms have higher energy than the displacement energy [79], referred to as ultra-shallow implantation or sub-plantation [74-76]. It allows the ions to pass through the surface and settle underneath it, and as a result, film growth can occur below and above the surface. Due to film-substrate intermixing and the creation of chemical bonds, the film can be well-adherent [70]. At the same time, films made by vigorous deposition can be incredibly defective and rigid and have high inherent stress. Excessive intrinsic stress results in catastrophic delamination failures, so the ion arrival energy is critical [70].

Some studies have found that when the kinetic of the condensing particles is between 5 and 25 electron volts, sub-plantation is insufficient, and development will occur on the surface of a film with significant adatom mobility [70]. Those particle energies are equal to substrate heating to a certain extent. As a result, adatom mobility will be increased, the film will be thick and well-textured, and flaws will be decreased considerably.

Natural kinetic energy, potential energy, energy due to a magnetic field, conduction band energy, sheath energy due to substrate bias, and other energies comprise an ion's overall energy carried to the surface [70].

Therefore, in addition to changing the plasma emission and magnetic field, changing the substrate bias is another method for adjusting ion arrival energy. This bias should be negative to the ions, and a substrate bias creates a thin space charge that can accelerate ions. Different ion charges will experience differential acceleration, which results in kinetic energy differences upon hitting the substrate. Although substrate bias is beneficial for developing a thick layer, a high substrate bias analogous to a strong magnetic field can result in ion reflection and the sputtering of energetic ions.

The final component that can impact film quality is substrate temperature. Adatoms' mobility and surface response increase as the temperature increases, which results in intense nucleation and film development. However, the deposited materials may re-evaporate if the surface temperature is too high [77].

2.5. High entropy nitrides (HEN)

2.5.1. Fundamentals of HEN

Multi-component nitride materials that add nitrogen to a HEA are called high entropy nitrides, and to understand the phase constancy and bonding of high-entropy nitrides following the introduction of nitrogen, knowledge of overall nitrogen-related interaction trend is required [16]. Figure 8 shows the capacity of transition metals to form not thermodynamically stable nitride series throughout the periodic table, finding strong nitride formers in groups 4-6. Groups 7-11 create weak nitrides or do not form nitrides [16].

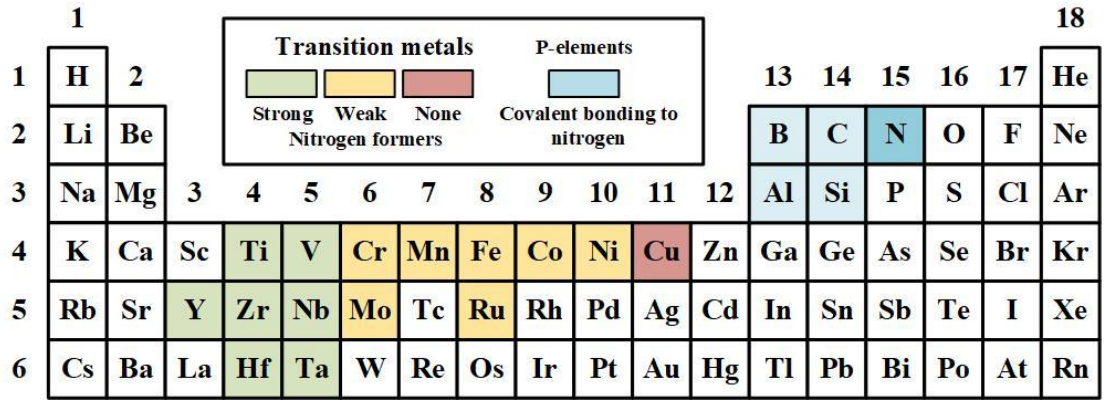

Figure 8. A Periodic table demonstrates the elements synthesising multi-component nitrides with simple crystal structures and their general nitrogen bonding capabilities [16].

Interstitial compounds are stable transition metal nitrides where non-metal atoms, such as N, fill crevices in the close-packing structure of metal [16]. It should be noted that these compounds' bonding and electrical structure differ from solid solutions of non-metals in metal phases. While non-metals have limited solubility in metal phases, almost 50% of the atoms in interstitial compounds are non-metal [16]. These compounds have crystal structures similar to NaCl (B1), in which octahedral structures surround both elements. Interstitial nitrides such as TiN are bonded in various ways, including covalent, metallic and ionic, which results in desirable properties such as increased hardness, electrical and thermal conductivity and comparable chemical stability. However, group 3 nitrides with the NaCl-type structure are semiconductors, which differs from group 4 and group 5 transition metal nitrides. Due to bonding and structural similarities, prolonged homogeneity zones exist for solid solutions of many binary transition metal nitrides, such as TiN and VN [78].

As the strength of the nitride bond between the transition metals decreases towards the right of the periodic table, the enthalpy of synthesis of NaCl-type nitrides also decreases, which results in the prevalence of alternative structures with other stoichiometries. As valence electron concentration increases, the filling of anti- and non-bonding electronic

states also increases. For example, FeN (H_f^0 = 47 kJ/mol) is substantially less stable than TiN (H_f^0 = 338 kJ/mol) [79]. In addition, several FeN_x compounds with different stoichiometries and crystal structures exist [79]. For instance, Cu_3N has a positive formation enthalpy that is metastable (H_f^0 = 71 kJ/mol) as one moves further towards the right of the periodic table [80]. H_f^0 (AlN) = 318 kJ/mol and H_f^0 (Si_3N_4) = 743 kJ/mol are exceptionally stable nitrides that are formed by group 13 and 14 elements Al and Si [81].

Covalent nitrides are known to be stable in hexagonal wurtzite (B4) and Si_3N_4 structures, as indicated by the blue part of Figure 8. Metal atoms surround N in a tetragonal fashion in each arrangement, while AlN and Si_3N_4 are connected to other p-element nitrides. As a result of bonding and structural differences, Al and Si do not show prolonged solubility in binary transition metal nitrides at thermodynamic equilibrium. However, adding silicon to titanium nitride leads to the formation of a nanocomposite structure that consists of nanocrystalline titanium nitride and an amorphous silicon nitride tissue phase, which is known as nc-TiN/a-Si_3N_4 [82]. For example, metastable solid solutions, cubic $(Ti_{1-x}Al_x)N$, may be synthesised under kinetically constrained conditions (e.g. vapour deposition methods) [83].

Based on previous research, expecting high entropy nitrides based on transition metals from the early stages of the transition to form solid solutions that are similar to NaCl is reasonable. However, nitrides with multiple components based on transition metals from the late or intermediate stage are more likely to form more intricate nitrides. Such complex structures are not anticipated from thin film deposition since the mobility of adatoms is limited during the growth of the vapour phase [84]. Therefore, the likelihood of amorphous structures forming from the vapour deposition of late or intermediate

transition metals in a nitride-forming environment is greater. The creation of structures when strong, weak, and non-nitride-forming metals are combined, or the impact increasing configurational entropy is not immediately apparent. However, some conclusions have been drawn from a preliminary study [16].

2.5.2. Current trends of high entropy nitrides

Chen et al. (2004) deposited coatings of nitride through sputtering from HEA targets, which resulted in amorphous coatings, as only metals with the capability of generating weak nitrides (Cr, Mn, Fe, Co, Ni, Cu) and Al were used [11]. More than 70 publications on multicomponent nitride coatings have since been published, 65 of which dealt with crystalline solid solution nitrides with many components and some with thin amorphous coatings as diffusion barriers [16]. Considerable debate has raged over the extent of the entropic stabilisation for HEA-based compounds, such as HEN [16]. It could be argued that only the metal sub-lattice contributes to enhanced configurational entropy in a stoichiometric multi-component complex through the random occupancy of at least five metallic elements. Conversely, the remaining sub-lattice is filled with N, for example, and contributes no entropy. Boltzmann's formula can explain this for configurational entropy in the case of a closed system [85]:

$$S_B = K_B \, ln \, (W)$$

Where S_B is the configurational entropy and K_B Is the number of potential microstates.

The number of alternative configurations for a specific number of metallic elements in a solid solution is independent of whether the voids of the structure are vacant (as in a HEA) or filled with nitrogen. However, in a stoichiometric nitrogen system, potential states increase due to unfilled voids, which may occupy different positions relative to the metallic elements. The configurational energy would then be increased. The

situation becomes increasingly complex with the consideration of an open system. Gibbs' formula for configurational entropy can be employed [16].

$$S_G = -k_B \sum_i (p_i ln\ (p_i))$$

Where p_i is the probability for each microstate and k_B is Boltzmann's constant.

The likelihood of each state is included in Gibbs' formula, and this allows for a range of entropy contributions for alloys and compounds, including nitrides, due to differing chemical interactions. Consequently, there is a varying likelihood of various microstates of metal atoms, particularly if the nitrogen affinity of metallic elements. This is of greater significance in sub-stoichiometric systems, where configurations with unfilled voids near metal atoms with low nitrogen affinity have a higher probability [16].

Therefore, when a closed system and a stoichiometric multi-component compound are considered, the entropy stabilisation should be the same as that of the equivalent alloy, as measured in metal atoms or nitride moles. The entropy may be different with non-stoichiometric molecules or open systems, but the degree and significance of this discrepancy are outside of the remit of this research [16]. It is important to emphasise that the entropic stabilisation of a multi-component oxide has been experimentally established. In addition, the stability of chemicals is determined by the "screening" of the metallic sublattice and consequent energy microstate degeneration. Therefore, entropy plays a role in the creation of phases of solid solution with a simple crystal structure in multicomponent compounds.

Transition metals and aluminium, silicon, carbon, and barium have been used for manufacturing multi-component nitride coatings [16]. The reported bulk

multicomponent nitrides have been synthesised using reactive sputter deposition with alloy targets and N_2 as the reactive gas. At the same time, CAD in an N_2 environment or sputtering from elemental or segmental targets are both equally feasible synthesis techniques. As determined by altering the partial pressure of nitrogen during synthesis, the nitrogen content is the most often studied compositional variation.

The metallic coatings of the researched systems are either amorphous or crystalline. A crystalline nitride phase is created when sufficient nitrogen is used in the synthesis process. Certain compositions have unambiguous combinations of metallic alloy and crystalline nitride phases as coatings [16]. Few studies have focused solely on materials composed of transition metals from the early stages, which are satisfied nitride formers and can generate extensive solid solution nitrides even when entropy stabilisation is absent. Most research has focused on materials that mix early and intermediate transition metals via intermediate nitride bonding and a strong covalent nitride-forming element. Some HENs have been shown to form metastable solid solutions when combined with TiN [16]. Other coatings that have been examined include Si, which is typically combined with Al and, in most instances, Cr. Only NaCl-type solid solution phases have been seen in nitride coatings, and their Bravais lattice generally identifies them - FCC structure.

Figure 9 shows the structural evolution of coatings in the (Al-Cr-Ta-Ti-Zr)N_x system as a function of nitrogen concentration. An FCC lattice compatible with a NaCl-type crystal structure may be observed with nitrogen concentrations of 14 per cent and N_2 in the process gas. The degree of favoured orientation and peak broadening varies when the quantity of N_2 is further increased, suggesting a decrease in grain size. Such microstructural alterations are prevalent in developing nitride coatings [86]. As seen in Figure 9, most evaluated HEN coatings include a significant proportion of components

that do not generate NaCl-type nitrides.

Nonetheless, with multi-component coatings, solid solution NaCl-type nitride phases develop. Dedoncke has studied coatings in the (Co-Cr-Cu-Fe-Ni)N_x system with no strong nitride formers. Cr is the only element in this system known to form a NaCl-type phase during vapour deposition, which provides the most severe demonstration of this [12]. This proves that multi-component nitride coatings can create basic crystal forms in solid solution phases. Two mechanisms contribute to stabilising the simple solid solution phase: the high-entropy effect associated with many components and a kinetic stabilisation based on restricted (surface) diffusion during development from the vapour phase. This also prefers crystal formations with simple crystal structures and solid solutions [84]. The expected slow diffusion effect for multi-component materials may amplify this impact.

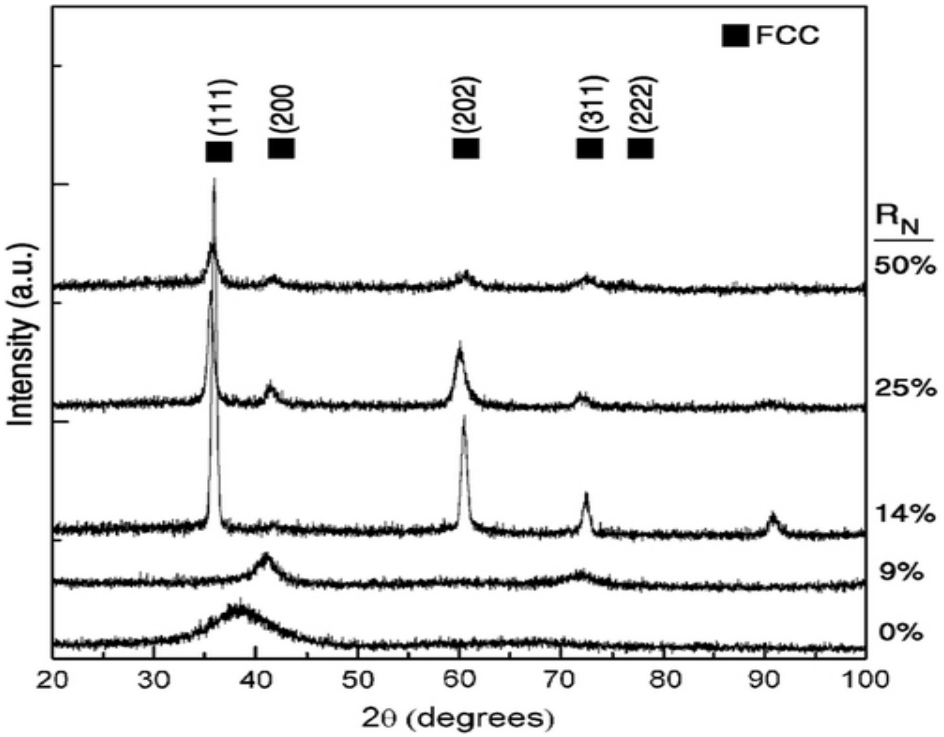

Figure 9. X-ray diffractograms of coatings in the (Al-Cr-Ta-Ti-Zr)Nx system demonstrate structural development as a function of nitrogen concentration [87]

2.5.3. $AlCrFeCoNiCu_{0.5}$ nitride thin film

According to research by Khan, some of the previous expectation has been proven for $AlCrFeCoNiCu_{0.5}$ nitride thin film [10]. The same radio frequency (RF) sputtering apparatus used for depositing his $AlCrFeCoNiCu_{0.5}$ HEA thin film samples was utilised, and $AlCrFeCoNiCu_{0.5}$ nitride thin films were deposited at a different flow ratio of $N/(N + Ar)$ (6.25 percent, 12.5 percent, and 25 percent) [10].

The crystallinity of HEN films changed from a combined cubic FCC and BCC condition to a partly amorphous condition as the nitrogen gas flow response increased. This was noticed as a substantial number of interstitial nitrogen atoms was collected in the film [10]. The scanning electron microscopy and atomic force microscopy results demonstrated that grain yield size and grain surface roughness were reduced [10]. At a nitrogen gas concentration of 25%, approximately 10.6% of nitrogen was deposited in the film. Significant surface protective oxides and nitrides were deposited on the HEN thin films at 12.5% and 25% nitrogen gas. When 25% nitrogen gas was introduced, the highest hardness of 9.8 GPA was attained, compared to 6.25% and 12.5% nitrogen gas [10].

Most published literature on HEN thin film fabrication shows that magnetron sputtering and the cathodic arc will give different results in chemical composition, crystal structure, physical properties, etc.

3. Methodology

3.1. Film fabrication

A filtered cathodic arc deposition (FCAD) SPArc system with a single circular cathode was used for depositing the $AlCrFeCoNiCu_{0.5}$ HEA and HEN thin films. A structural diagram of the FCAD was shown in supplementary materials (see Figure S1). The cathode had a purity of 99.9% with a diameter of 44 mm and thickness of 33 mm. A copper anode with an inner diameter of 50.8 mm, an outside diameter of 54 mm, and a length of 41 mm was positioned concentrically outside the HEA cathode [17]. The protrusion of the anode was 8 mm higher than the surface of the cathode and faced the filter chamber. A half-semicircle torus current carrying coil (duct) with 22.5 turns, 440 mm in radius and 140 mm in cross-sectional diameter, was used to create a magnetic field to guide the plasma discharged from the cathode to the substrate. Commercial Si (100) wafers were used as the film substrates. Each substrate was cleaned at least three times for 5 minutes in an ultrasonic solution of acetone, ethanol and deionised water. The chamber was pre-pumped to an average base pressure of 0.0005 Pa prior to depositions. Each deposition comprised 10,000 arc current pulses with a pulse length of 600 μs and a frequency of 5 Hz. The quantity of plasma deposited on the substrate and the capability to filter the plasma were determined by the arc current and magnetic filter duct current, which were set as 900 A and 420 A, respectively. The pressure during deposition was controlled by regulating the nitrogen gas flowrate via a mass flow controller. Table 1 shows the nitrogen flowrate of each deposition and the corresponding working pressure.

Table 1. Nitrogen flowrate with corresponding working pressure for each deposition.

Sample	Nitrogen Flow Rate (sccm)	Pressure (Pa)
HEA	0.00	0.0005
0.005 Pa	0.52	0.005
0.01 Pa	1.17	0.01
0.05 Pa	6.17	0.05

3.2. Profilometer

A DektakXT stylus profilometer (Bruker USA) was used for measuring the thickness of the film. Deep valleys from the substrate to the thin films were created using a physical mask applied on the substrate before deposition, and more details of this process are shown in the supplementary materials (Figure S2). The thickness of each thin film was then measured 20 times at five separate points along the length of each valley using a scanning length of 1000 μm and a 7 mg stylus force. The scanning speed was set at 10 μm/s with a resolution of 0.1 μm/pt.

3.3. Transmission Electron Microscopy (TEM)

Scanning transmission electron microscopy - energy dispersive x-ray spectroscopy (STEM-EDS) and high-resolution transmission electron microscopy (HRTEM) were applied to analyse the cross-sectional chemical composition and microstructure of the thin films, respectively. Zeiss Auriga focused ion beam (FIB) was used for preparing the cross-sectional TEM specimens. Molybdenum (Mo) grids were used to replace the conventional copper (Cu) grids to prevent counts from the grid interfering with the Cu signal from the samples, as Cu is one of the major elements in the thin film system. The microscope FEI Themis Z equipped with four ChemiSTEM (Super-X) EDS detectors

was used to perform HRTEM and STEM-EDS at the accelerating voltage of 300 KV, and the 400pA beam current was set during EDS mappings acquisition. The EDS data and TEM images were processed using Velox (Thermo Fisher Scientific Inc.) and Digital Micrograph software (Gatan Inc.), separately.

3.4. X-ray photoelectron spectroscopy (XPS)

The surface chemical state of the HEN thin films was investigated using a Thermo K-Alpha$^+$ X-ray photoelectron spectroscopy (XPS) equipped with a monochromatic Al Kα radiation which has a wavelength of 0.83 nm and a probe size of 400 μm. Ar^+ etching at 300 eV for 30 seconds, with an estimated etching rate of 0.12 nm/s for Si, was set to eliminate surface contamination prior to XPS composition measurements. Another 120 s Ar^+ etching was set to remove any oxidation layers on the surface. The X-ray source was operated at 12 kV and 6 mA. Survey spectra were recorded using scan step sizes of 1 eV, and high-resolution spectra were recorded using a scan step size of 0.1 eV. XPS data were analysed using Origin and Avantage surface analysis software.

3.5. X-ray diffraction (XRD)

A structural investigation of thin films was performed using an X'Pert Powder X-ray diffractometer (XRD) that was set up with a copper X-ray source and typical Bragg-Brentano geometry. The working voltage was set at 45 kV, and the current was set at 40 mA. A scan range of between 20° and 90° and a resolution of 0.0131° were utilised for analysing each thin film. The XRD data were analysed using Origin and PDF-4$^+$ software, and the phase structure was identified by X'pert Highscore software.

3.6. Atomic Force Microscopy (AFM)

A Bruker AFM was used for measuring the surface roughness of the thin films in contact mode over a scanning area of 1 μm x 1 μm. The scan rate was set at 1 Hz, and the

amplitude setpoint voltage was 250 mV. NanoScope Analysis software was utilised to process three-dimensional (3D) topographical images and determine the average roughness of the thin films.

3.7. Nanoindentation

A Hysitron TI 850 Tribo Indenter was used to determine each thin film's hardness and elastic modulus. A Berkovich indenter tip with a radius of 150 nm was employed for the measurements, and a load of up to 5000 μN was applied to each thin film. The contact depth was controlled within 10% of the thickness of each thin film to minimise the influence of the substrate on the measurements [88]. The average hardness and elastic modulus values for each thin film were calculated after performing 16 indents with a spacing of 10 μm to avoid interactions between indentations.

4. Results and discussion

4.1. Film thickness and deposition rate

A profilometer was used to study the influence of nitrogen pressure on the thickness and deposition rate of each thin film. The thickness and deposition rate of each $AlCrFeCoNiCu_{0.5}$ HEA and HEN thin film, deposited at various nitrogen deposition pressures, are shown in Figure 10. The HEA thin film, with an average thickness of 420.0 ± 20.6 nm, had the lowest deposition rate of 12.6 ± 0.6 nm/min. Upon introducing nitrogen gas into the chamber, no statistically significant increase in the deposition rate was observed as the pressure increased up to 0.01 Pa. However, at a pressure of 0.05 Pa, a significantly higher deposition rate of 33.4 ± 1.0 nm/min was observed, producing a film with a thickness of 1175.8 ± 33.4 nm. This observation could be potentially attributed to the reduced backscattering and self-sputtering. Backscattering occurred when energetic adatoms were reflected after impacting on the film surface during

deposition, whereas self-sputtering occurred when surface atoms were ejected from the growing film after a collision with an incoming energetic adatom, thereby etching the atoms on the film surface [18]. When nitrogen was introduced into the chamber, collisions between the plasma and gas molecules caused energy exchange, which resulted in a reduction of ion kinetic energies [89]. As nitrogen pressure increased, the probability of plasma species encountering collisions on their way to the substrate increased [89, 90]. Therefore, the rates of backscattering and self-sputtering would be reduced, leading to an increase in the deposition rate. The mean free path (λ) of depositing species is given by [91]

$$\lambda = \frac{k_B T}{\sqrt{2}\pi d^2 p}$$

where k_B is the Boltzmann constant (1.380649×10^{-23} J/k), T is the temperature, d is the kinetic diameter of the gas molecule, p is the pressure. At the pressure of 0.05 Pa, the mean free path between collisions was calculated to be 0.14 m, indicating the collisions per depositing specie was expected to be 100 times higher than that of HEA thin film ($\lambda = 14.0$ m) during deposition. Therefore, it could significantly decrease the impact energy of the depositing flux, which led to the increase in the deposition rate of the HEN thin film.

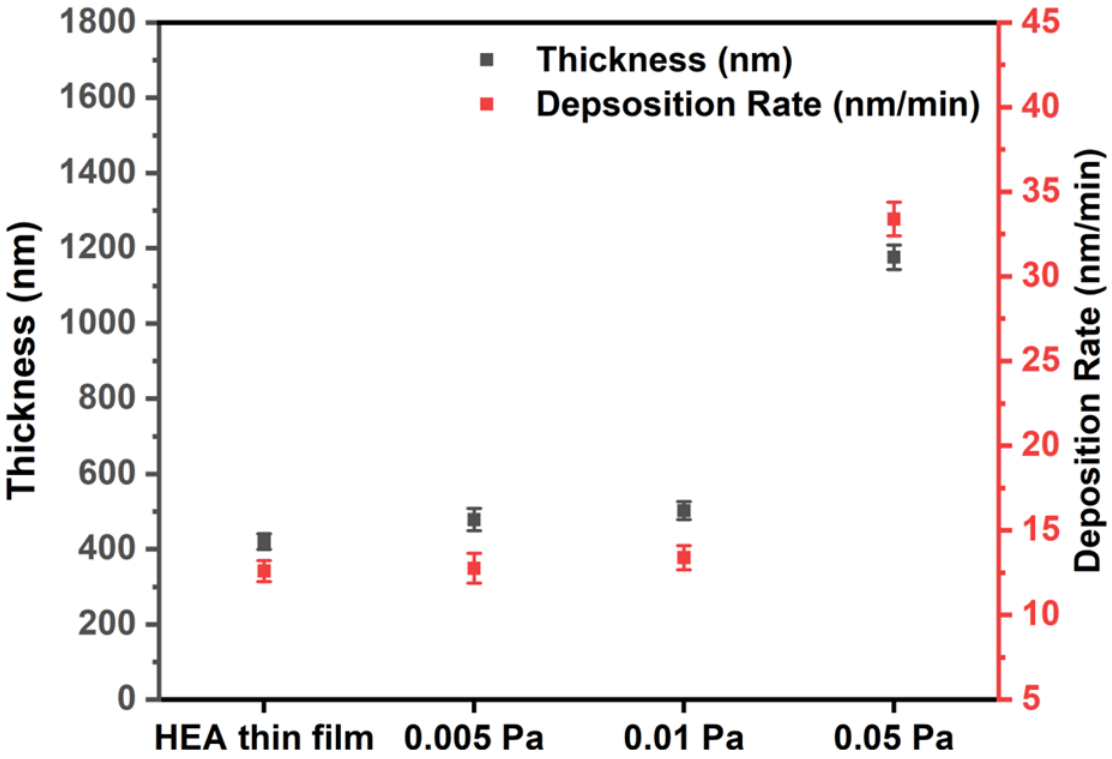

Figure 10. Thickness and deposition rate of each $AlCrFeCoNiCu_{0.5}$ HEA and HEN thin film fabricated at various nitrogen pressures.

4.2. Chemical Composition

STEM-EDS was performed to investigate the evolution of the chemical composition in the HEA and HEN thin films with the increasing nitrogen pressure. The cross-sectional elemental distribution of each thin film can be seen in Figure 11. It was clearly observed that aluminium was segregated from the other elements above the interface between thin film and substrate. We suspected that when energetic aluminium ions bombarded the surface, the Al_2O_3 compound formed due to the oxygen-enriched layer on the substrate surface [18]. Therefore, the sputtering yield of aluminium near the surface was reduced due to the higher surface binding energy of Al_2O_3 compared to the crystalline HEA [92]. When the pressure increased, the effect of the sputtering of aluminium decreased due to energy loss. Thus, the difference in sputtering yield decreased. In addition, the formation of AlN also lowered the sputtering yield of the aluminium due to strong covalent bonds between aluminium and nitrogen. Therefore,

the segregation of aluminium reduced when the pressure increased. As a result, the aluminium distribution was homogenous at 0.05 Pa. Additionally, all the films exhibited a homogeneous elemental distribution throughout their thickness, benefiting from the rapid quenching effect during thin film growth [93]. Nitrogen was observed to be well distributed into the HEN thin films deposited at 0.005 Pa, 0.01 Pa and 0.05 Pa.

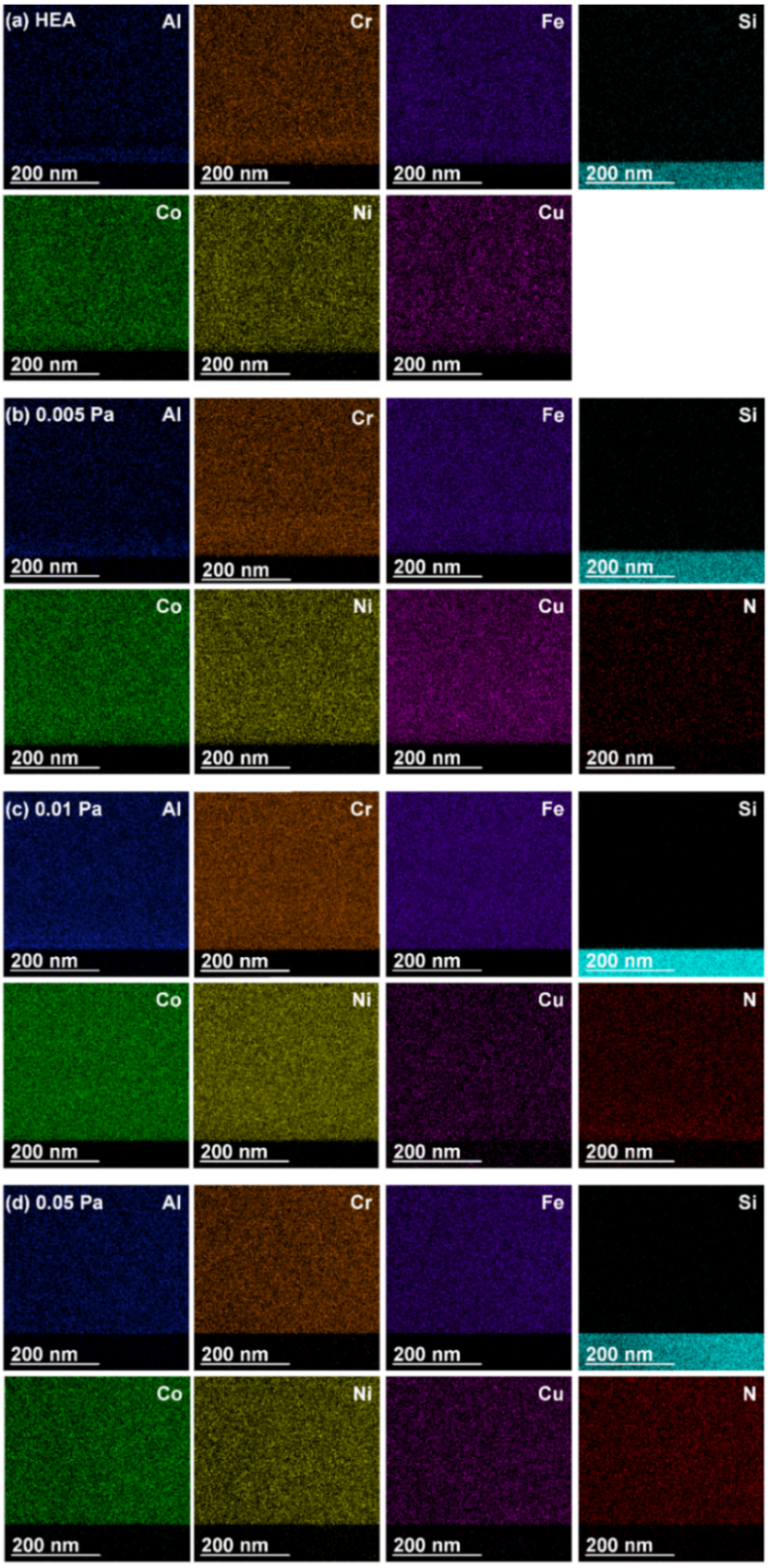

Figure 11. Cross-sectional STEM-EDS mapping of each HEA and HEN thin film deposited at various pressures. (a) HEA thin film; (b), (c) and (d) HEN thin films deposited at 0.005 Pa, 0.01 Pa and 0.05 Pa, respectively.

The chemical composition of thin films measured by STEM-EDS is shown in Figure 12. The nitrogen concentration of the HEN thin films increased from 4.3 ± 0.3 at. % to 21.2 ± 1.1 at. % when the pressure increased from 0.005 Pa to 0.05 Pa. The increasing nitrogen concentration was suspected as a result of enhanced reactivity when energetic ions collided with nitrogen molecules along their paths to the substrate due to the increased nitrogen content. This will be discussed in section 4.3. Note that, the aluminium concentration in the thin films ranged from 8.3 ± 1.5 at. % to 12.9 ± 2.2 at. %, which was lower than that of HEA target. When the pressure increased to 0.05 Pa, there was a decrease of 5 at.% for the other five elements except for Al because of the increased nitrogen concentration. When energetic heavy metal ions bombarded the film surface during deposition, preferential sputtering could occur [94]. Therefore, the lighter elements (Al) were likely to have experienced preferentially sputtering. Higher ion energies at lower working pressures led to lower aluminium concentration [94]. When the pressure significantly increased, collisions between the gas molecules and the plasma stream would reduce the ion kinetic energy [89], thereby reducing the effect of preferential sputtering and causing a relative increase in aluminium concentration in the HEN thin films at 0.01 Pa and 0.05 Pa.

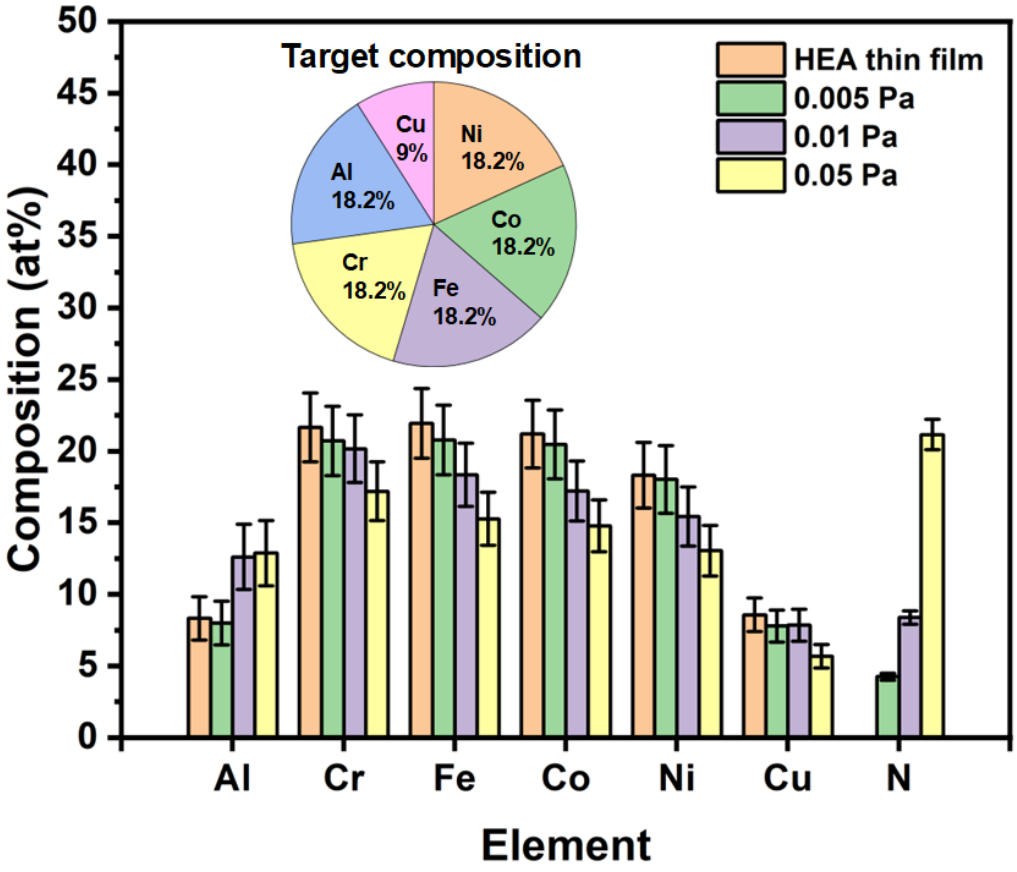

Figure 12. Chemical composition of the $AlCrFeCoNiCu_{0.5}$ HEA and HEN thin films deposited at different pressures measured via STEM-EDS

4.3. Surface chemistry

XPS was utilised to analyse the surface chemistry and reactivity of each metallic element with nitrogen. The survey spectra are shown in the supplementary information (see Figure S3). Figure 13 presents high-resolution XPS patterns of metal elements in each thin film on the surface. The Al_{2s} spectra were selected to prevent overlap with the Cu_{3p} signal. The XPS patterns of Al_{2s} and Cr_{2p} in Figure 13 (a) and (b) reveal different oxidation states on all thin films according to the appearance of the Al_2O_3 and Cr_2O_3 peaks. Since there was no signal of AlN and CrN observed at 0.005 Pa, the nitrogen content detected by STEM-EDS (4.3 ± 0.3 at. %) was thought to be stored in but not chemically bonded into the thin film. When the nitrogen pressure increased to 0.01 Pa, AlN and CrN peaks started to appear. No metallic aluminium peak was observed in the

thin film deposited at 0.05 Pa, while chromium remained partially in the metallic state. Only metallic peaks were observed in Fe_{2p}, Co_{2p}, Ni_{2p} and Cu_{2p} spectra, indicating that only the metallic phase of these elements exists in each film. The lower reactivity of Fe, Co, Ni and Cu with nitrogen could be explained by their higher formation enthalpy, as summarised in Table 2. A broad peak between $Fe_{2p1/2}$ and $Fe_{2p3/2}$ in Figure 13 (a) was potentially due to peak overlaps with Cu LMM, Co LMM and Ni LMM [18].

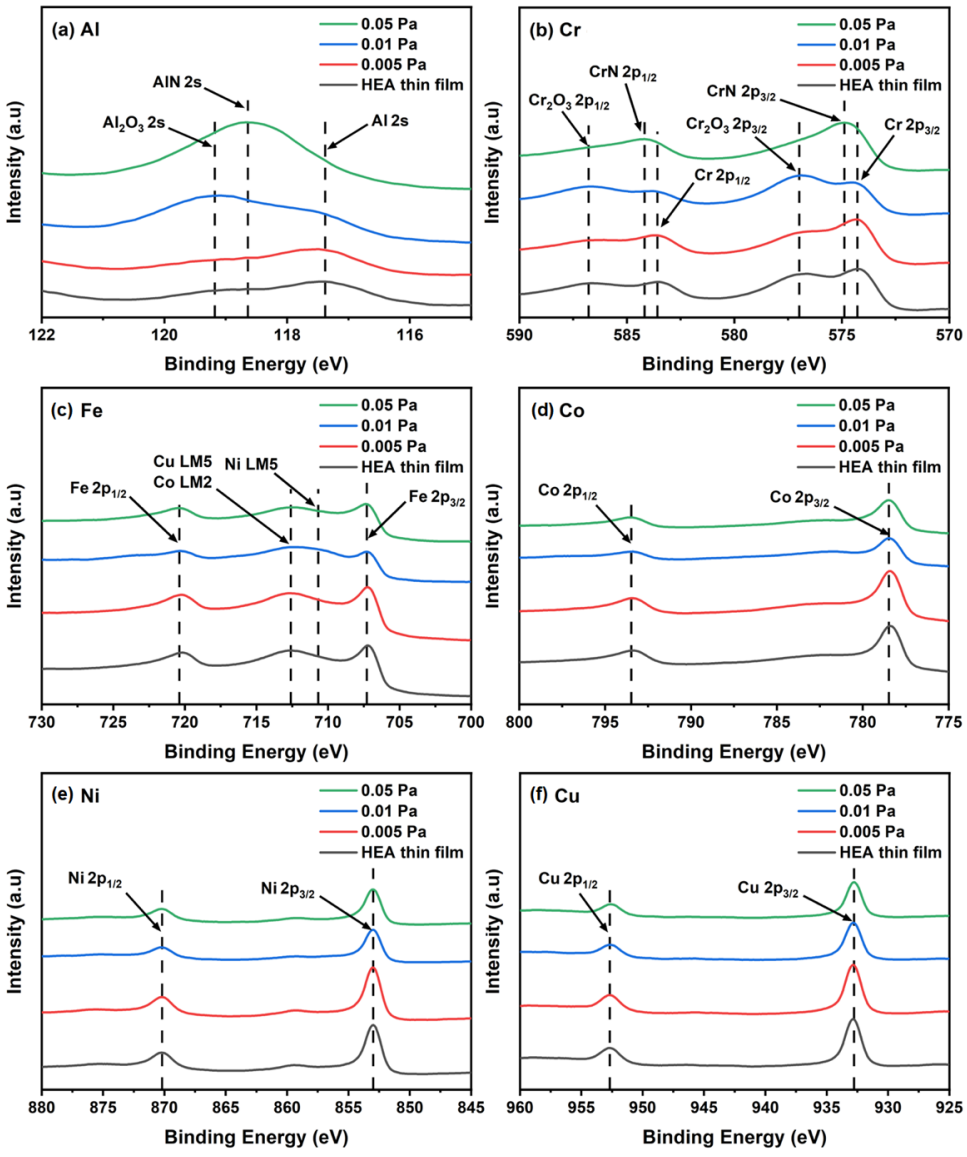

Figure 13. High-resolution XPS spectra of (a) Al, (b) Cr, (c) Fe, (d) Co, (e) Ni, and (f) Cu presenting on the surface of each AlCrFeCoNiCu0.5 HEA and HEN thin film fabricated at various nitrogen pressures.

Table 2. Standard enthalpy of formation (ΔH_f^0) for binary nitride of each metallic element in AlCrFeCoNiCu system at 298 K [95-97].

Compound	ΔH_f (kJ/mol)
AlN	-317.98
CrN	-117.15
Fe2N	+12.60
Co3N	+8.40
Cu3N	+74.50
Ni3N	N/A

The high-resolution XPS patterns of aluminium, chromium and nitrogen beneath the surface are shown in Figure 14 (a), (b) and (c), respectively. The absence of Al_2O_3 and Cr_2O_3 peaks in the Al_{2s} and Cr_{2p} spectra shown in Figure 14 (a) and (b) indicated the oxidation of Al and Cr only occurred on the film surface, most likely due to post-deposition atmospheric reactions. The AlN peak remained after etching, while no CrN peaks were detected in any of the HEN thin films, indicating that the CrN only formed on the surface of the thin films. In Figure 14 (c), no AlN or CrN peaks in the thin film fabricated at 0.005 Pa further proved that the nitrogen beneath the film surface was not chemically bonded in the thin film. The preferential formation of AlN in the HEN thin films could be explained by its lower enthalpy of formation. Aluminium has 3 outer shell valence electrons, while chromium has 6 valence electrons. When chromium reacts with nitrogen (having 5 valence electrons), it can lose 6 electrons to form Cr_2N (ΔH_f^0)= -125.52 kJ/mol) [96] to achieve the stable electron configuration or lose 1 electron to form CrN (H_f^0) = -117.15 kJ/mol) [96]. In contrast, aluminium can lose 3 electrons easily to achieve the noble gas electron configuration, and form stable nitride

with an enthalpy of formation (ΔH_f^0)) of -317.98 kJ/mol [16, 96], which is more stable than Cr_2N and CrN. Therefore, based on thermodynamics, AlN preferred to form rather than these two chromium nitrides.

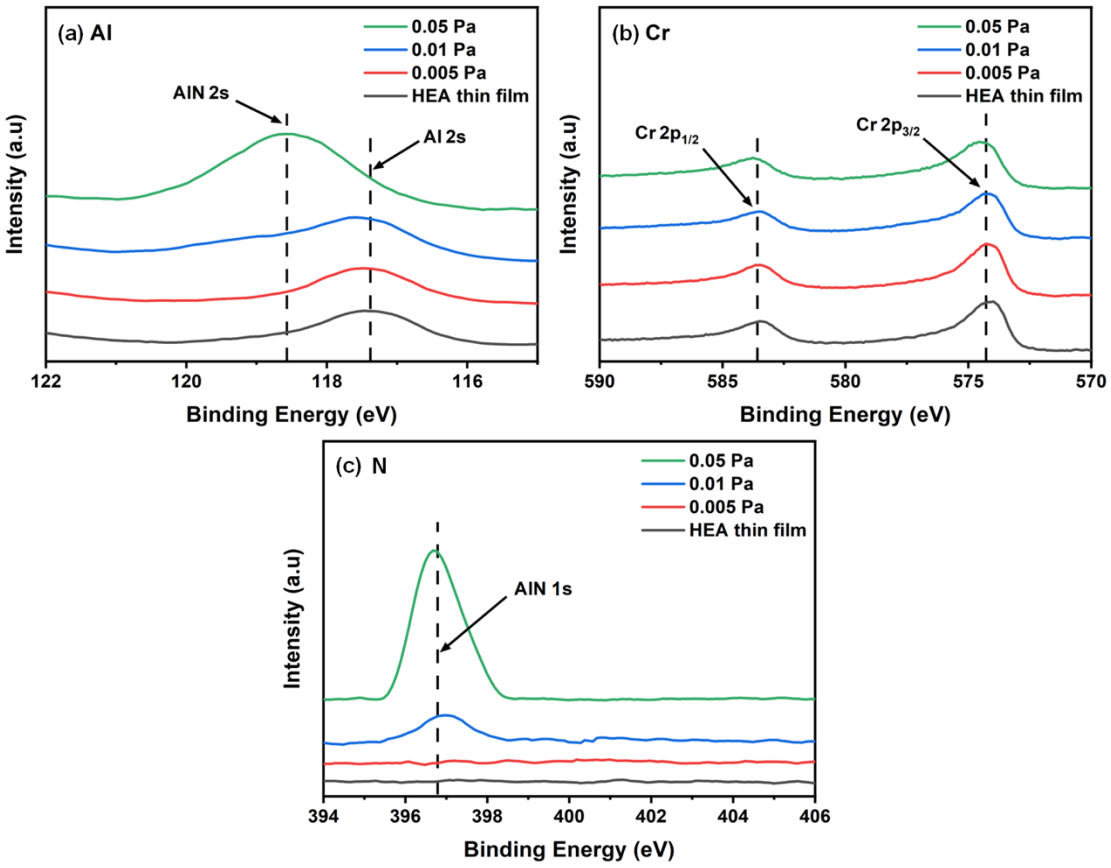

Figure 14. High-resolution XPS spectra of Al_{2s} and Cr_{2p} for each $AlCrFeCoNiCu_{0.5}$ HEA and HEN thin film on the surface and after 120s of Ar etching.

4.4. Crystallography and microstructure

The crystalline structure of the thin films deposited at various pressures was investigated by XRD. The XRD patterns in the range of 2θ from 30° to 60° are plotted in Figure 15. Patterns collected across the range from 20° to 90° are shown in the supplementary information (see Figure S4). The peak at 46.1° in Figure 15 was indexed as SiO_2 (111) [98] on the substrate surface. Also, an unknown peak at 47.8° was observed in the XRD pattern of the substrate (see Figure S4). The phase of $AlCrFeCoNiCu_{0.5}$ HEA thin film was identified as a single FCC based on the strong

(111) peak indexed at 43.4° [99-101]. The formation of the FCC phase was attributed to the low concentration of Al in the thin films (~ 9.5 at. %). It has been reported that a typical face-centred cubic (FCC) phase is more favourable to form in the AlCrFeCoNiCu system when the aluminium concentration is less than 10 at. % [17, 32, 33]. Increasing signs of amorphisation in the HEN thin films were observed with increasing nitrogen pressure. Table 3 summarises the calculated lattice constants based on the XRD results. The slight left-hand shift of the FCC peak from the HEA thin film to the HEN thin film deposited at 0.005 Pa indicates a slight increase in lattice constant from 3.607 Å to 3.630 Å, which is due to more severe lattice distortion resulting from the incorporation of some interstitial nitrogen [102]. The lattice constant then decreased to 3.581 Å at 0.01 Pa because of the contraction of the lattice caused by the formation of stronger covalent bonds between aluminium and nitrogen [16].

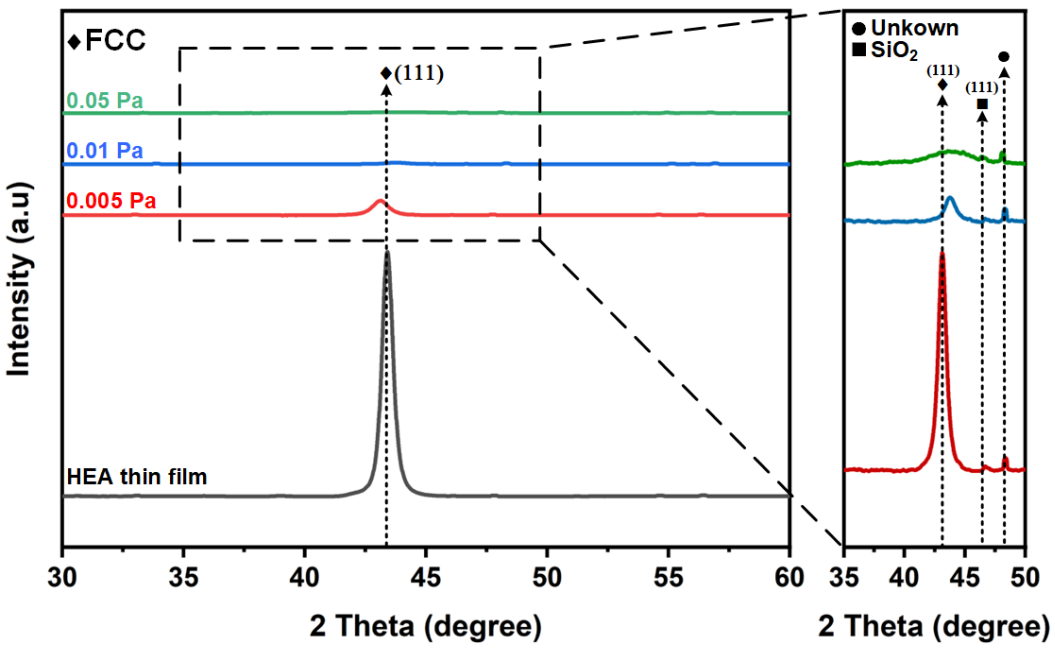

Figure 15. XRD pattern for each $AlCrFeCoNiCu_{0.5}$ HEA and HEN thin film deposited at various nitrogen pressure by CAD.

Table 3. Lattice parameters of the $AlCrFeCoNiCu_{0.5}$ HEA and HEN thin films deposited at various pressures.

	2θ (°)	Lattice constant (Å)
HEA thin film	43.423	3.607
0.005 Pa	43.121	3.630
0.01 Pa	43.746	3.581
0.05 Pa	N/A	N/A

The evolution of microstructure in the thin films at various pressures was revealed by HRTEM. Figure 16 (a), (c), (e) and (g) show the cross-sectional morphology of thin films at low magnification. A clear columnar structure can be observed for the pressure of 0.01 Pa, while the film deposited at 0.05 Pa possesses a homogenous structure. Figure 16 (b), (d), (f) and (h) show the microstructure of the thin films. A single FCC phase with a (111) spacing of 0.208 nm was indexed in the HEA thin film. Then the FCC (111) spacing decreased to 0.206 nm when the pressure increased to 0.01 Pa. The fully amorphised HEN thin film deposited at 0.05 Pa demonstrated that the regular lattice spacing had been disrupted by more severe lattice distortion as more interstitial sites were occupied by nitrogen [34, 35]. In addition, high pressure at 0.05 Pa also strengthened isotropy. The microstructure of the thin films and the varied FCC (111) spacing performed in HRTEM showed good agreement with the observation from XRD results.

The average grain sizes of the thin films are summarised in Table 4. It is clear that the grain size decreased when pressure increased up to 0.01 Pa. The smaller average grain size at 0.005 Pa (69.5 nm ± 23.1 nm × 23.9 nm ± 6.2 nm) compared to that of the HEA thin film (135.9 nm ± 35.3 nm × 42.1 nm ± 12.7 nm) is believed to result from a reduced

nucleation density. The decreasing tendency of the grain size with increasing pressure could be explained by energy-dependent nucleation and growth. When the nitrogen gas was not present during the deposition, more energetic ions bombard the surface, causing thermal spikes [93, 103]. The thermal spikes on the surface result in high surface diffusivity of adatoms, inhibiting atoms from condensing and nucleation. Therefore, the grain size would be relatively larger due to the lower nucleation density. However, smaller thermal spikes would be created with the increasing pressure as impacting ion energies are reduced. Thus, the surface mobility of adatoms was reduced, reducing the grain size. When the pressure increased to 0.005 Pa, collisions between metallic ions and gas molecules increased. Then the impacting ion kinetic energy was reduced[104], and the surface adatom mobility was decreased[18]. Consequently, more nucleation sites formed, hindering the growth of large crystal grains [21]. The average grain size further decreased to 32.4 nm ± 16.4 nm in length and 17.4 nm ± 4.7 nm in width at 0.01 Pa, which was consistent with a further reduction in adatom impact energy. The interstitial nitrogen and strong covalent bonds might also hinder the diffusion of surface atoms [1], which could further limit grain growth. We suspected that the amorphous regions observed at 0.01 Pa, which can inhibit the movement of grain boundaries, might also create a barrier to grain growth [90].

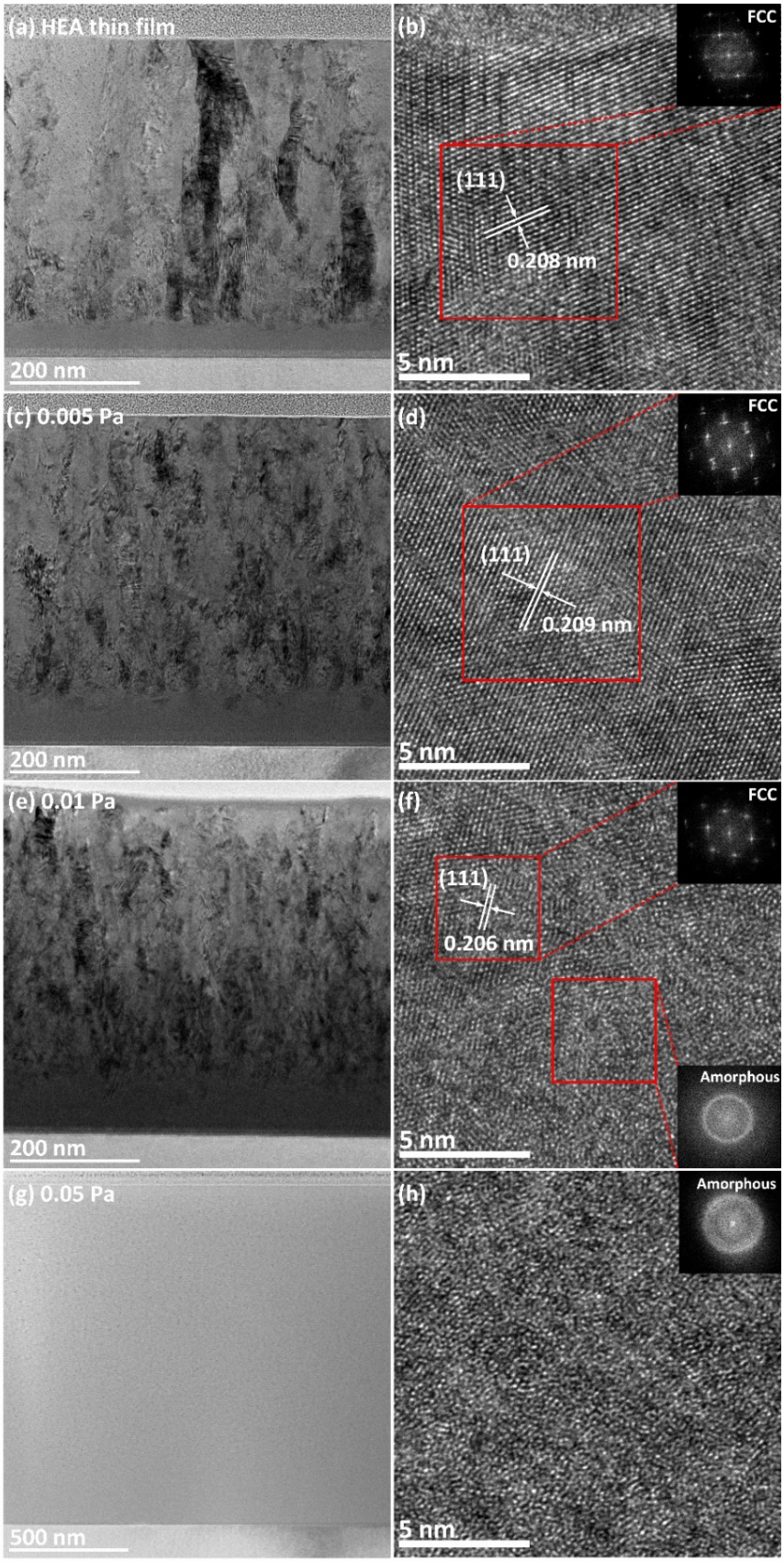

Figure 16. Cross-sectional TEM images and HRTEM images of $AlCrFeCoNiCu_{0.5}$ HEA (a) and (b) and HEN thin films deposited at 0.005 Pa (c) and (d), 0.01 Pa (e) and (f), and 0.05 Pa (g) and (f), respectively.

Table 4. Grain sizes of the thin films deposited at various pressures.

	HEA thin film	0.005 Pa	0.01 Pa	0.05 Pa
Grain length (nm)	135.9 ± 35.3	69.5 ± 23.1	32.4 ± 16.4	N/A
Grain width (nm)	42.1 ± 12.7	23.9 ± 6.2	17.4 ± 4.7	N/A

4.5. Mechanical properties

Nanoindentation was performed to investigate the hardness and elastic modulus and observe the correlation between microstructure and mechanical properties. The hardness and elastic modulus of each thin film are shown in Figure 17. The HEA thin film exhibited an average hardness of 6.7 ± 0.5 GPa and an average elastic modulus of 150.0 ± 11.5 GPa. It is observed that each HEN thin film possessed higher hardness and elastic modulus than those of the HEA thin film. Several strengthening mechanisms were introduced in the HEN thin films. The enhanced hardness (8.4 ± 0.7 GPa) and elastic modulus (198.2 ± 17.9 GPa) at 0.005 Pa can be due to the interstitial solid solution structure. The atomic radius of the nitrogen atom is significantly smaller than that of the metallic atoms in the AlCrCoFeNiCu system [105]. The filling of interstitial sites occupied by smaller nitrogen in crystal lattice caused more severe lattice distortion, enhancing the internal strain, which would impede the formation and movement of dislocations [102]. The hardness and elastic modulus of the thin film deposited at 0.01 Pa increased to 9.7 ± 0.6 GPa and 230.2 ± 11.8 GPa, respectively. The improvement of the mechanical properties at 0.01 Pa could be explained by the increased interatomic force. Strong covalent bonds formed between aluminium and nitrogen impeded the atomic rearrangement and deformation, leading to the improvement of mechanical properties [106]. The highest value of hardness (12.4 ± 0.6 GPa) and elastic modulus

(347.3 ± 17.7 GPa) at 0.05 Pa might be due to the fully amorphous structure. The findings of hardness and elastic modulus evolution were consistent with most reported HEN thin films. As nitrogen pressure increased, there was a transition from the FCC phase into an amorphous structure with increased nitrogen content [10, 107]. The maximum hardness and elastic modulus of the HEN films fabricated by RF magnetron sputtering were only 9.8 ± 0.8 GPa and 149 ± 5.1 GPa, respectively [10]. In comparison, the HEN thin films presented in this work exhibited significantly better mechanical properties.

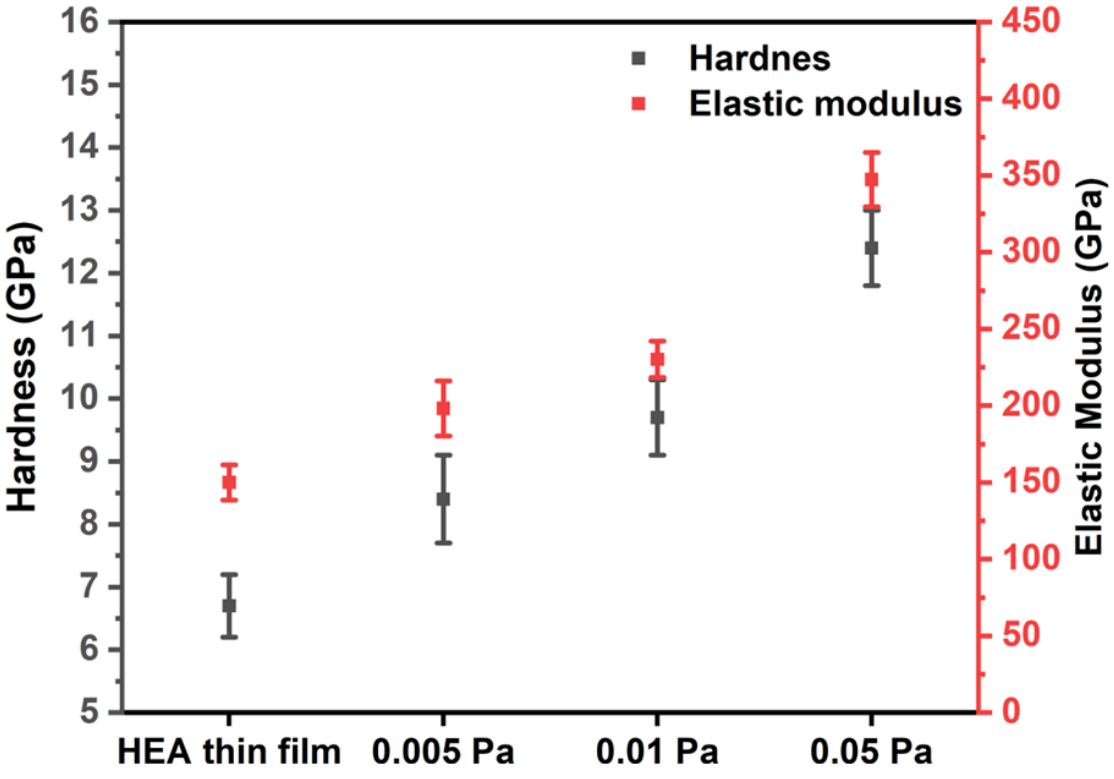

Figure 17. Hardness and elastic modulus of each $AlCrFeCoNiCu_{0.5}$ HEA and HEN thin film fabricated at various pressures.

Figure 18 plots the hardness and elastic modulus for the reported $AlCrFeCoNiCu_{0.5}$ HEA thin film fabricated by magnetron sputtering and cathodic arc deposition and $AlCoCrCu_{0.5}FeNi$ nitride thin films deposited by cathodic arc. The present work of $AlCrFeCoNiCu_{0.5}$ nitride deposited by cathodic arc deposition showed a significant

improvement in hardness and elastic modulus from its HEA thin films and exhibited superior mechanical properties compared to most of the multi-component nitride thin films consisting of similar elements.

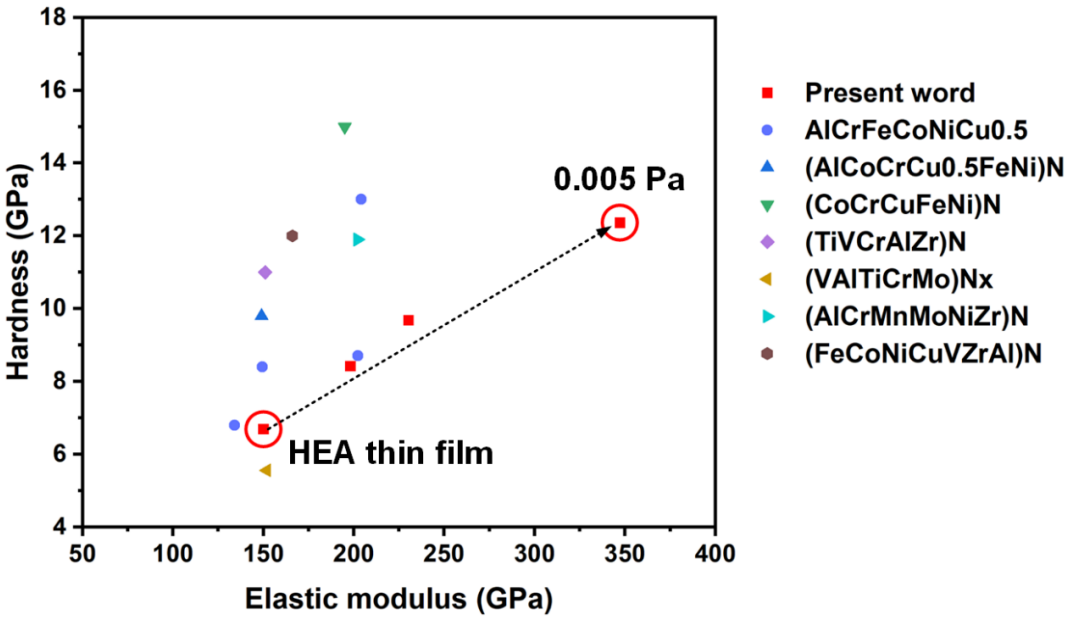

Figure 18. Mechanical properties of some reported AlCrFeCoNiCu0.5 HEA thin films deposited by RF sputtering [7, 53] and cathodic arc deposition [17, 93, 108-110]*, AlCoCrCu0.5FeNi nitride deposited by RF sputtering [10] and some reported HEN thin films, (CoCrCuFeNi)N* [111]*, (TiVCrAlZr)N* [112]*, (VAlTiCrMo)Nx)* [113]*, (AlCrMnMoNiZr)N* [114] *and (FeCoNiCuVZrAl)N [9].*

4.6. Surface morphology

The surface morphology and roughness of the thin films deposited at various pressures were studied with AFM. The scanned surfaces of thin films deposited at various pressures are shown in Figure 19. The surface roughness (R_q) of the HEA thin film was 0.7 nm, increasing slightly to 0.9 nm in the thin film deposited at 0.005 Pa. The increase in surface roughness of the thin film deposited at 0.005 Pa was due to the reduced surface mobility caused by energy loss when energetic ions collided with gas molecules [89]. When the pressure increased to 0.01 Pa, the combination of the FCC phase and amorphous structure was suspected to be the main reason for the significant increase in surface roughness to 2.6 nm. The lowest roughness of 0.2 nm was observed in the

amorphous film deposited at 0.05 Pa due to its homogenous structure.

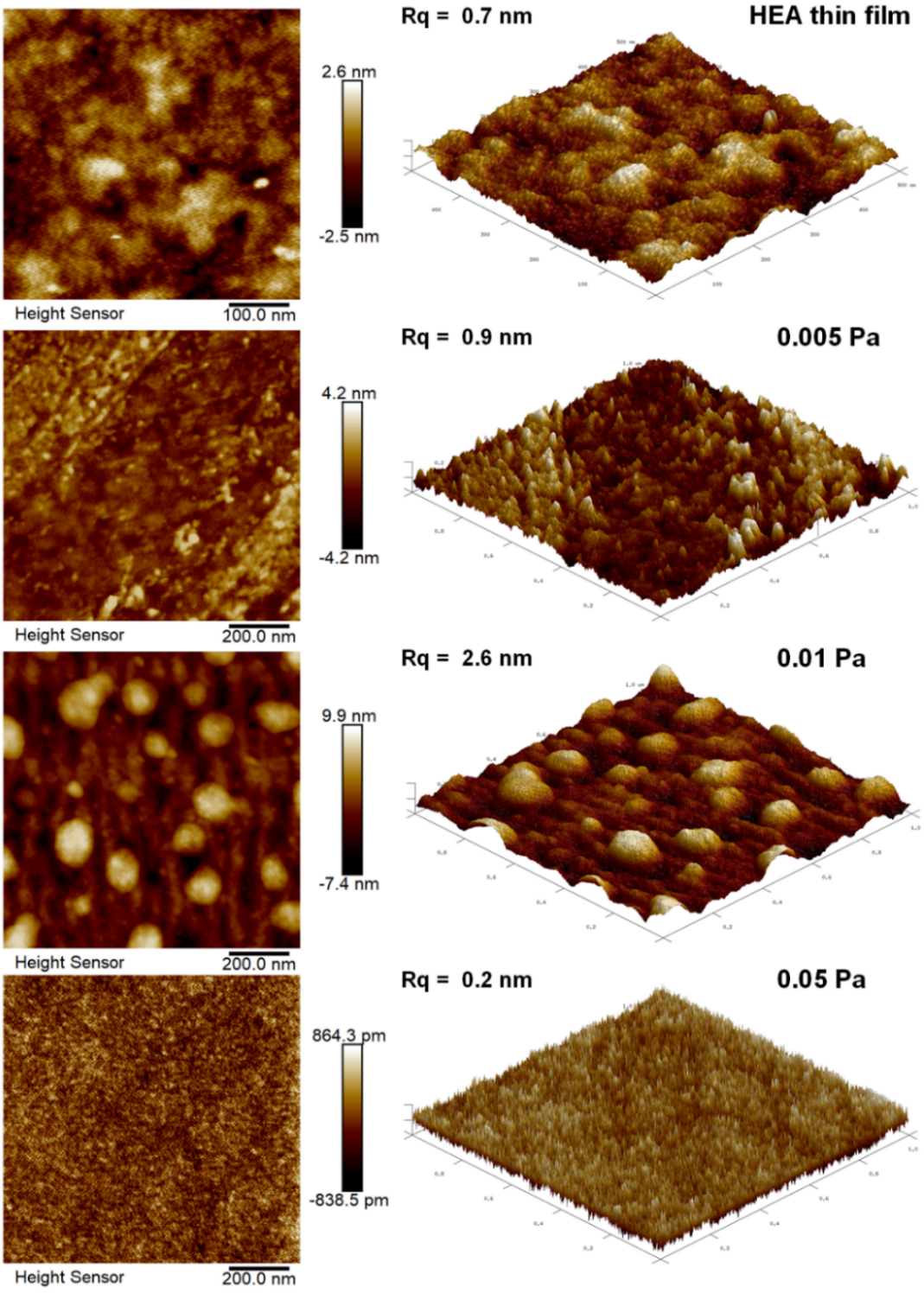

Figure 19. Surface morphology and roughness of each $AlCrFeCoNiCu_{0.5}$ HEA and HEN thin film deposited at various pressures determined by AFM.

5. Conclusions and Recommendations

In conclusion, a new deposition technique with controllable microstructure was developed to synthesise $AlCrFeCoNiCu_{0.5}$ HEA and HEN thin films. The microstructure and chemistry of the thin films were controlled by tuning pressure during thin film fabrication to achieve the enhancement of mechanical properties. The main findings are summarized below.

(1) The deposition rate increased as the increase of pressure because of the weakened backscattering and self-sputtering effects. The highest deposition rate reached 33.4 ± 1.0 nm/min.

(2) Both HEA and HEN thin films exhibited uniform elemental distribution, which was mainly due to the rapid quenching effect during deposition. The lower Al atomic concentration was caused by the preferential sputtering.

(3) XPS results revealed a "naturally" formed oxidation layer of Al_2O_3 and Cr_2O_3 on the top surface of each thin film. The preferential formation of AlN was due to its lower formation enthalpy.

(4) There was a phase transition of HEN thin films from single FCC phase to amorphous when the pressure increased from 0.005 Pa to 0.05 Pa. The grain size of the films was decreased by the limited surface adatom mobility due to the decreasing ion kinetic energy at higher pressure.

(5) Interstitial nitrogen solid solution, amorphous and the formation of covalent bonds could greatly contribute to the improvement of hardness and elastic modulus. The thin film deposited at 0.05 Pa with complete amorphous structure showed the highest hardness of 12.4 ± 0.2 GPa and elastic modulus of 347.3 ± 17.7 GPa. These values were 84.8% and 131.4% higher than those of the HEA thin film.

Continuous investigation of high entropy nitride thin films is essential to developing various application fields for multi-component materials. Even though this study provides crucial insights into the fabrication, microstructure, and mechanical properties of $AlCrFeCoNiCu_{0.5}$ HEN thin films under various pressures, there is still much to investigate. The complexity of multi-component materials and their potential for various applications indicate the requirement for additional comprehensive and systematic research. Future research can investigate a variety of fabrication and performance related parameters to determine how they affect the properties of the films. This would entail tuning the deposition process, investigating various film configurations, experimenting with post-deposition procedures, and evaluating film performance under various conditions. Future research can build on the findings of this study and advance the understanding and potential applications of $AlCrFeCoNiCu_{0.5}$ HEN thin films with the aid of the investigations.

5.1. Property tests

5.1.1. Wear test

$AlCrFeCoNiCu_{0.5}$ HEN thin films surface are recommended as protective coatings suitable for aerospace applications [10], which require high resistance to material loss or deformation under stress in settings where the materials are subjected to regular or intense friction. Evaluation of the durability and performance of materials under various operational conditions relies on wear testing. The wear mechanisms can be studied in detail with various wear tests offering a deeper understanding of how these thin films behave under stress. Several typical types of wear are considered to be tested and are informed in the following sections.

Abrasive wear

Abrasive wear refers to the wear mechanism as a result of the disintegration of the material on the surface due to the influence of the hard particle in contact with the surface. It also occurs when a hard surface or particles interact with or slide on a flexible surface, leading to the loss of material [115].

Adhesive wear

Adhesive wear refers to unwanted displacement and attachment of wear debris and material compounds from one surface to another and can be found between surfaces during frictional contact [116]. The surface layers can deform very small fragments, with the surface roughness affecting the severity of how fragments of nitrides are pulled off and added to the other surface. This type of adhesive wear can result from strong adhesive forces between atoms [117] or energy accumulation in the deformation zone between the asperities during relative.

Fatigue wear

Fatigue wear is a type of wear in which the surface of the material is damaged due to strain induced on the surface for a specific number of cycles up to a critical limit. The mechanism of fatigue wear formation begins with the formation of cracks and fissures on the surface of the material; the crack generated on the surface is the consequence of external conditions such as sliding or rolling on the surface [118]. Since this wear is determined by the mechanics of fracture formation, which is induced by high levels of strain, the microstructure of the material's surface is altered, influencing the wear processes [115].

Fretting wear

Fretting wear is a destructive phenomenon that occurs when two contacting surfaces undergo relative motion with minute displacement under load [119]. The fretting attrition causes significant material degradation and surface fatigue. The degradation mechanism is unique and is largely disregarded. Comparatively, less wear occurs under significantly fewer sliding conditions; however, at a certain point, the sliding is sufficient to effect microscopic surface changes due to changes in normal and tangential loads; these surface changes cause fretting wear [120].

Erosion wear

Erosive wear can be defined as the degradation of a material due to the impact of particles travelling with significant velocity [121]. The objects or particles that cause erosive wear refer to eroding particles, significantly impacting the extent of erosive wear. The various physical and chemical characteristics of the eroding particles influence the formation and occurrence of erosive wear. Surface protective coatings on aerospace applications, such as gas turbine blades, are susceptible to erosive attrition when subjected to the constant influence of the external environment [122].

Corrosion wear

Corrosion wear refers to chemical wear caused by chemical and electrochemical reactions between the surface and the environment [123]. This type of corrosion can result from corroding mediums such as chemical agents, lubricants or atmospheric mediums [124]. Since wear and corrosion processes characterise this deterioration, the affected material would endure severe damage or loss [122].

5.2. Fabrication process

The fabrication procedure substantially impacts the properties of high entropy nitride thin films, and a number of variables could be investigated further to optimise these advanced materials. Future research could considerably contribute to developing and applying high entropy nitride thin films if it thoroughly investigates these fabrication-related aspects.

5.2.1. Substrate bias

Appling a substrate bias can adjust the ion energy. Different ion charges can experience differential acceleration affected by the thin space charge created by the negative substrate bias [20]. The increase in ion kinetic energy causes heat accumulation on the surface, increasing the mobility of adatoms on the surface. Hence, the nucleation sites can be decreased, forming larger crystal grains [102]. Enhanced substrate bias has been reported to have the ability to affect the microstructure and the interface between the thin film and substrate of multi-component coatings fabricated by cathodic arc deposition and improve their mechanical properties [18, 125]. However, a strong substrate bias can increase backscattering and self-sputtering, which reduces deposition efficacy, and it can also increase backscattering. Additionally, the preferential sputtering of lighter elements will be enhanced, and the varying concentration of elements in the AlCrFeCoNiCu system can alter the crystal structure. Therefore, substrate bias is worth to be studied in the fabrication of $AlCrFeCoNiCu_{0.5}$ HEN thin films.

5.2.2. Substrate temperature

The temperature of the substrate during the deposition process is an additional crucial parameter that can significantly affect the properties of HEN thin films. The deposition temperature governs many aspects of thin film growth, including adatom mobility,

surface diffusion, nucleation rate, and phase formation, all of which significantly impact the thin films' microstructure [21]. It has been found that the increasing substrate temperature frequently results in increased adatom mobility, which can facilitate the development of larger, better-defined crystalline grains, thereby enhancing the film's structural integrity and possibly its mechanical properties [126]. Therefore, the substrate temperature is a potential field to improve the quality of $AlCrFeCoNiCu_{0.5}$ HEN thin films, which should be further studied.

5.2.3. Nitrogen fraction

In this study, the nitrogen content of $AlCrFeCoNiCu_{0.5}$ HEN thin films was governed by the deposition pressure in nitrogen gas. Therefore, the concentration of nitrogen in the thin film and the nitrogen pressure affected the growth and microstructure of the thin film. However, the HEN thin film can also be deposited using a combination of nitrogen and another noble gas at a constant pressure. In this instance, the nitrogen concentration in HEN thin films can be modulated by adjusting the nitrogen fraction, which reveals the effect of nitrogen content in thin films.

5.2.4. Different substrate

High entropy nitride thin film fabrication and efficacy are greatly influenced by the substrate material chosen. It influences numerous characteristics of the thin film, such as adhesion strength, crystal orientation, film tension, and interfacial reactions, which directly affect the film's overall properties and reliability. However, most of the research is limited to depositing thin films on Si wafers and Al_2O_3, which may not be the actual substrate that needs to be coated for the application [106, 127].

Due to their distinct physical and chemical properties, different substrate materials can affect the film differently. For instance, a substrate with a different thermal expansion

coefficient may cause varying levels of film stress, which can impact the film's mechanical stability. In addition, the substrate's surface roughness and chemical reactivity can impact the film's nucleation and growth mechanisms, thereby influencing its microstructure and phase formation. $AlCrFeCoNiCu_{0.5}$ HEN thin films deposited on commonly used application materials, such as stainless steel, should be studied.

5.3. Post-treatment

Post-deposition treatments are a potent method for modifying and fine-tuning the properties of thin high-entropy nitride films. These procedures, which can include annealing, ion implantation, and laser treatment, can alter a film's microstructure, phase, and surface characteristics, resulting in changes to its properties.

Annealing can promote grain growth, reduce defects, and stabilise the structure of the film, thereby potentially increasing its hardness and wear resistance. It may also result in phase transformations. AlCrFeCoNiCu system has reported that the microstructure and phases can be altered via annealing and reinforced by multi-phase hardening and nanotwins [109]. It is suspected that annealing can also induce a phase transition in the nitride thin film of this system, affecting the mechanical properties of the thin films. Ion implantation can introduce dopants or generate a surface layer with altered properties, whereas laser treatments can alter the interface composition [21]. Each of these treatments offers high tunability over the film's properties, as they can be precisely controlled to achieve specific results.

To sum up, $AlCrFeCoNiCu_{0.5}$ HEN thin film has great potential in aerospace protective coating applications due to its weak chemical reactivity and enhanced mechanical properties compared to its HEA thin film. However, the study of $AlCrFeCoNiCu_{0.5}$ HEN is still limited. Other properties, such as wear resistance, should also be tested. To

fabricate reinforced $AlCrFeCoNiCu_{0.5}$ HEN thin films, the effect of substrate bias, substrate temperature and nitrogen fraction in noble gas is also worth investigating. Different materials used for actual applications should also be considered as a substrate further to evaluate the performance of $AlCrFeCoNiCu_{0.5}$ HEN thin film.

Reference

[1] J.-W. Yeh *et al.*, "Nanostructured High-Entropy Alloys with Multiple Principal Elements: Novel Alloy Design Concepts and Outcomes," *Advanced Engineering Materials,* vol. 6, pp. 299-303, 05/01 2004, doi: 10.1002/adem.200300567.

[2] S.-y. Yen, Y.-c. Liu, S.-h. Chu, C.-w. Chang, S.-k. Lin, and M.-H. Tsai, "B2-strengthened Al-Co-Cr-Fe-Ni high entropy alloy with high ductility," *Materials Letters,* vol. 325, p. 132828, 2022/10/15/ 2022, doi: https://doi.org/10.1016/j.matlet.2022.132828.

[3] H.-S. Do, T. J. Jang, K. J. Kim, S. S. Sohn, and B.-J. Lee, "A novel high-entropy alloy with multi-strengthening mechanisms: Activation of TRIP effect in C-doped high-entropy alloy," *Materials Science and Engineering: A,* vol. 859, p. 144220, 2022/11/24/ 2022, doi: https://doi.org/10.1016/j.msea.2022.144220.

[4] Z. Cheng *et al.*, "Studies on high-temperature stability and strengthening mechanisms of high/medium-entropy alloys for potential nuclear applications: The case of FeCrV-based alloys," *Materials Science and Engineering: A,* p. 144858, 2023/02/27/ 2023, doi: https://doi.org/10.1016/j.msea.2023.144858.

[5] Z. Tang *et al.*, "Aluminum Alloying Effects on Lattice Types, Microstructures, and Mechanical Behavior of High-Entropy Alloys Systems," *JOM,* vol. 65, no. 12, pp. 1848-1858, 2013/12/01 2013, doi: 10.1007/s11837-013-0776-z.

[6] E. J. Pickering, A. W. Carruthers, P. J. Barron, S. C. Middleburgh, D. E. J. Armstrong, and A. S. Gandy, "High-Entropy Alloys for Advanced Nuclear Applications," *Entropy,* vol. 23, no. 1, p. 98, 2021. [Online]. Available: https://www.mdpi.com/1099-4300/23/1/98.

[7] N. A. Khan *et al.*, "RF magnetron sputtered AlCoCrCu0.5FeNi high entropy alloy (HEA) thin films with tuned microstructure and chemical composition," *Journal of Alloys and Compounds,* vol. 836, p. 155348, 2020/09/25/ 2020, doi: https://doi.org/10.1016/j.jallcom.2020.155348.

[8] A. Rashidy Ahmady, A. Ekhlasi, A. Nouri, M. Haghbin Nazarpak, P. Gong, and A. Solouk, "High entropy alloy coatings for biomedical applications: A review," *Smart Materials in Manufacturing,* vol. 1, p. 100009, 2023/01/01/ 2023, doi: https://doi.org/10.1016/j.smmf.2022.100009.

[9] L. Liu, J. B. Zhu, C. Hou, J. C. Li, and Q. Jiang, "Dense and smooth amorphous films of multicomponent FeCoNiCuVZrAl high-entropy alloy deposited by direct current magnetron sputtering," *Materials & Design (1980-2015),* vol. 46, pp. 675-679, 2013/04/01/ 2013, doi: https://doi.org/10.1016/j.matdes.2012.11.001.

[10] N. A. Khan *et al.*, "High entropy nitride (HEN) thin films of AlCoCrCu0.5FeNi deposited by reactive magnetron sputtering," *Surface and Coatings Technology,* vol. 402, p. 126327, 2020/11/25/ 2020, doi: https://doi.org/10.1016/j.surfcoat.2020.126327.

[11] T. K. Chen, T. T. Shun, J. W. Yeh, and M. S. Wong, "Nanostructured nitride films of multi-element high-entropy alloys by reactive DC sputtering," *Surface*

and Coatings Technology, vol. 188-189, pp. 193-200, 2004/11/01/ 2004, doi: https://doi.org/10.1016/j.surfcoat.2004.08.023.

[12] R. Dedoncker *et al.*, "Reactive sputter deposition of CoCrCuFeNi in nitrogen/argon mixtures," *Journal of Alloys and Compounds,* vol. 769, pp. 881-888, 2018/11/15/ 2018, doi: https://doi.org/10.1016/j.jallcom.2018.08.044.

[13] B. Ren, S. Q. Yan, R. F. Zhao, and Z. X. Liu, "Structure and properties of (AlCrMoNiTi)Nx and (AlCrMoZrTi)Nx films by reactive RF sputtering," *Surface and Coatings Technology,* vol. 235, pp. 764-772, 2013/11/25/ 2013, doi: https://doi.org/10.1016/j.surfcoat.2013.08.064.

[14] B. B. Straumal *et al.*, "High Entropy Alloys Coatings Deposited by Laser Cladding: A Review of Grain Boundary Wetting Phenomena," *Coatings,* vol. 12, no. 3, p. 343, 2022. [Online]. Available: https://www.mdpi.com/2079-6412/12/3/343.

[15] Q. Zhang, Q. Wang, B. Han, M. Li, C. Hu, and J. Wang, "Comparative studies on microstructure and properties of CoCrFeMnNi high entropy alloy coatings fabricated by high-speed laser cladding and normal laser cladding," *Journal of Alloys and Compounds,* vol. 947, p. 169517, 2023/06/25/ 2023, doi: https://doi.org/10.1016/j.jallcom.2023.169517.

[16] E. Lewin, "Multi-component and high-entropy nitride coatings—A promising field in need of a novel approach," *Journal of Applied Physics,* vol. 127, no. 16, p. 160901, 2020, doi: 10.1063/1.5144154.

[17] H. Zhao *et al.*, "Cathodic arc deposition of high entropy alloy thin films with controllable microstructure," *Surfaces and Interfaces,* vol. 37, p. 102692, 2023/04/01/ 2023, doi: https://doi.org/10.1016/j.surfin.2023.102692.

[18] H. Zhao *et al.*, "The fabrication and growth mechanism of AlCrFeCoNiCu0.5 HEA thin films by substrate-biased cathodic arc deposition," *Scientific Reports,* vol. 13, no. 1, p. 198, 2023/01/05 2023, doi: 10.1038/s41598-022-26232-9.

[19] J. Hu, X. Tian, H. Liu, C. Gong, and B. Wang, "Enhancement of discharge and deposition rate by imposed pulse current during the cathodic arc deposition of ta-C films," *Vacuum,* vol. 193, p. 110515, 2021/11/01/ 2021, doi: https://doi.org/10.1016/j.vacuum.2021.110515.

[20] A. Anders, "Chapter 10 - Unfiltered and Filtered Cathodic Arc Deposition," in *Handbook of Deposition Technologies for Films and Coatings (Third Edition)*, P. M. Martin Ed. Boston: William Andrew Publishing, 2010, pp. 466-531.

[21] D. M. Mattox, "Chapter 10 - Atomistic Film Growth and Some Growth-Related Film Properties," in *Handbook of Physical Vapor Deposition (PVD) Processing (Second Edition)*, D. M. Mattox Ed. Boston: William Andrew Publishing, 2010, pp. 333-398.

[22] M. Tsai and J.-W. Yeh, "High-Entropy Alloys: A Critical Review," *Materials Research Letters,* vol. 2, pp. 107-123, 04/02 2014, doi: 10.1080/21663831.2014.912690.

[23] D. B. Miracle and O. N. Senkov, "A critical review of high entropy alloys and related concepts," *Acta Materialia,* vol. 122, pp. 448-511, 2017/01/01/ 2017,

doi: https://doi.org/10.1016/j.actamat.2016.08.081.

[24] Y. A. Cengel, & Boles, M. A., *Thermodynamics: an engineering approach*, 8th ed. McGraw-Hill Education, 2014.

[25] F. Otto, Y. Yang, H. Bei, and E. P. George, "Relative effects of enthalpy and entropy on the phase stability of equiatomic high-entropy alloys," *Acta Materialia,* vol. 61, no. 7, pp. 2628-2638, 2013/04/01/ 2013, doi: https://doi.org/10.1016/j.actamat.2013.01.042.

[26] J.-W. L. Yeh, P.-K.; Chuang, W.-T., *High-Entropy Alloys: Fundamentals and Applications*. Springer, 2016.

[27] Z. Li, K. G. Pradeep, Y. Deng, D. Raabe, and C. C. Tasan, "Metastable high-entropy dual-phase alloys overcome the strength–ductility trade-off," *Nature,* vol. 534, no. 7606, pp. 227-230, 2016/06/01 2016, doi: 10.1038/nature17981.

[28] A. Inoue, "Stabilization of metallic supercooled liquid and bulk amorphous alloys," *Acta Materialia,* vol. 48, no. 1, pp. 279-306, 2000/01/01/ 2000, doi: https://doi.org/10.1016/S1359-6454(99)00300-6.

[29] A. Hirata *et al.*, "Direct observation of local atomic order in a metallic glass," *Nature Materials,* vol. 10, no. 1, pp. 28-33, 2011/01/01 2011, doi: 10.1038/nmat2897.

[30] R. Shannon, "Revised effective ionic radii and systematic studies of interatomic distances in halides and chalcogenides," *Acta Crystallographica Section A,* vol. 32, no. 5, pp. 751-767, 1976, doi: doi:10.1107/S0567739476001551.

[31] Y. F. Ye, Q. Wang, J. Lu, C. T. Liu, and Y. Yang, "High-entropy alloy: challenges and prospects," *Materials Today,* vol. 19, no. 6, pp. 349-362, 2016/07/01/ 2016, doi: https://doi.org/10.1016/j.mattod.2015.11.026.

[32] M. C. Gao, Yeh, J. W., Liaw, P. K., & Zhang, Y., *High-entropy alloys: fundamentals and applications*. Springer, 2018.

[33] Z. Wu, H. Bei, F. Otto, G. M. Pharr, and E. P. George, "Recovery, recrystallization, grain growth and phase stability of a family of FCC-structured multi-component equiatomic solid solution alloys," *Intermetallics,* vol. 46, pp. 131-140, 2014/03/01/ 2014, doi: https://doi.org/10.1016/j.intermet.2013.10.024.

[34] J. Kitagawa, S. Hamamoto, and N. Ishizu, "Cutting Edge of High-Entropy Alloy Superconductors from the Perspective of Materials Research," *Metals,* vol. 10, no. 8, p. 1078, 2020. [Online]. Available: https://www.mdpi.com/2075-4701/10/8/1078.

[35] O. N. Senkov, G. B. Wilks, D. B. Miracle, C. P. Chuang, and P. K. Liaw, "Refractory high-entropy alloys," *Intermetallics,* vol. 18, no. 9, pp. 1758-1765, 2010/09/01/ 2010, doi: https://doi.org/10.1016/j.intermet.2010.05.014.

[36] Y. Zhang *et al.*, "Microstructures and properties of high-entropy alloys," *Progress in Materials Science,* vol. 61, pp. 1-93, 2014/04/01/ 2014, doi: https://doi.org/10.1016/j.pmatsci.2013.10.001.

[37] F. J. Neto Antão, "HEAs: High Entropy Alloys for advanced systems and engines Examination Committee," 2020.

[38] S. Ranganathan, "Alloyed pleasures: Multimetallic cocktails," *Current Science,* vol. 85, 11/25 2003.

[39] W.-R. Wang, W.-L. Wang, and J.-W. Yeh, "Phases, microstructure and mechanical properties of AlxCoCrFeNi high-entropy alloys at elevated temperatures," *Journal of Alloys and Compounds,* vol. 589, pp. 143-152, 2014/03/15/ 2014, doi: https://doi.org/10.1016/j.jallcom.2013.11.084.

[40] D. M. Mattox, *Handbook of Physical Vapor Deposition (PVD) Processing*, Second ed. Oxford, UK: Elsevier, 2010.

[41] I. Petrov, "Microstructural evolution during film growth," *Journal of Vacuum Science & Technology A,* vol. 21, p. S117, 2003, doi: https://doi.org/10.1116/1.1601610.

[42] H. A. Jehn, "Nucleation and Growth of Thin Films," in *Advanced Techniques for Surface Engineering* H. A. J. Wolfram Gissler Ed., 1992, pp. 5–29.

[43] Y. Kajikawa, "4 - Analysing surface roughness evolution in thin films," in *Thin Film Growth*, Z. Cao Ed.: Woodhead Publishing, 2011, pp. 60-82.

[44] D. M. Mattox, "Surface cleaning in thin film technology," *Thin Solid Films,* vol. 53, no. 1, pp. 81-96, 1978/08/15/ 1978, doi: https://doi.org/10.1016/0040-6090(78)90376-0.

[45] H. J. Griesser, Ed. *Thin Film Coatings for Biomaterials and Biomedical Applications* (Woodhead Publishing Series in Biomaterials. Sawston, Cambridge, UK: Woodhead Publishing, 2016.

[46] P. G. Shewmon, "Thin films-interdiffusion and reactions," in *Thin films-interdiffusion and reactions*, K. N. T. J. M. Poate, and J. W. Mayer, Eds. Ed. New York: Wiley-Interscience, 1978, p. 578.

[47] B. Pieraggi, "2 - Diffusion and solid state reactions," in *Developments in High Temperature Corrosion and Protection of Materials*, W. Gao and Z. Li Eds.: Woodhead Publishing, 2008, pp. 9-35.

[48] A. M. Anders, P. M., *Handbook of Deposition Technologies for Films and Coatings (Third Edition)*. Boston: William Andrew Publishing, 2010.

[49] , "HANDBOOK OF CRYSTAL GROWTH," in *Fundamentals*, D. T. J. Hurle Ed. Amsterdam: Elsevier, 1993, p. ii.

[50] T. P. Bertelli *et al.*, "Magnetic anisotropy of Co thin films: Playing with the shadowing effect, magnetic field and substrate spinning," *Journal of Magnetism and Magnetic Materials,* vol. 426, pp. 636-640, 2017/03/15/ 2017, doi: https://doi.org/10.1016/j.jmmm.2016.10.157.

[51] S. Benhenda, J. M. Guglielmacci, M. Gillet, L. Hultman, and J. E. Sundgren, "Effect of substrate bias on the protective properties of TiN films grown by reactive magnetron sputtering onto Cu substrates," *Applied Surface Science,* vol. 40, no. 1, pp. 121-128, 1989/11/01/ 1989, doi: https://doi.org/10.1016/0169-4332(89)90166-9.

[52] M. M. M. Bilek and D. R. McKenzie, "A comprehensive model of stress generation and relief processes in thin films deposited with energetic ions,"

Surface and Coatings Technology, vol. 200, no. 14, pp. 4345-4354, 2006/04/10/ 2006, doi: https://doi.org/10.1016/j.surfcoat.2005.02.161.

[53] N. A. Khan *et al.*, "High entropy alloy thin films of AlCoCrCu0.5FeNi with controlled microstructure," *Applied Surface Science,* vol. 495, p. 143560, 2019/11/30/ 2019, doi: https://doi.org/10.1016/j.apsusc.2019.143560.

[54] T. Liao *et al.*, "Effect of V on microstructure, wear and corrosion properties in AlCoCrMoVx high entropy alloy coatings by laser cladding," *Journal of Materials Research and Technology,* 2023/02/19/ 2023, doi: https://doi.org/10.1016/j.jmrt.2023.02.098.

[55] X. Shang *et al.*, "Laser cladding [Cr–Fe4Co4Ni4]Cr2.6-xAlxMo0.4 high-entropy alloy coating to strong-acid erosion," *Intermetallics,* vol. 156, p. 107847, 2023/05/01/ 2023, doi: https://doi.org/10.1016/j.intermet.2023.107847.

[56] C. Deng, C. Wang, L. Chai, T. Wang, and J. Luo, "Mechanical and chemical properties of CoCrFeNiMo0.2 high entropy alloy coating fabricated on Ti6Al4V by laser cladding," *Intermetallics,* vol. 144, p. 107504, 2022/05/01/ 2022, doi: https://doi.org/10.1016/j.intermet.2022.107504.

[57] W. Li, P. Liu, and P. K. Liaw, "Microstructures and properties of high-entropy alloy films and coatings: a review," *Materials Research Letters,* vol. 6, no. 4, pp. 199-229, 2018/04/03 2018, doi: 10.1080/21663831.2018.1434248.

[58] X. H. Yan, J. S. Li, W. R. Zhang, and Y. Zhang, "A brief review of high-entropy films," *Materials Chemistry and Physics,* vol. 210, pp. 12-19, 2018/05/01/ 2018, doi: https://doi.org/10.1016/j.matchemphys.2017.07.078.

[59] J. Huebner, R. Pawel, D. Kata, and J. Kusinski, "Microstructural and Mechanical Study of Inconel 625 – Tungsten Carbide Composite Coatings Obtained by Powder Laser Cladding," *Archives of Metallurgy and Materials,* vol. 62, pp. 529-536, 05/15 2017, doi: 10.1515/amm-2017-0078.

[60] Z. Liu, "4.09 - Laser Applied Coatings," in *Shreir's Corrosion*, B. Cottis *et al.* Eds. Oxford: Elsevier, 2010, pp. 2622-2635.

[61] M. M. T. Hassan, A., in *Handbook of Antimicrobial Coatings*: Elsevier, 2018, pp. 321-355.

[62] J. J. C. Stephen M. Rossnagel, William D. Westwood, *Handbook of Plasma Processing Technology*. CRC Press, 1990.

[63] N. A. Khan, "RF Magnetron Sputtered AlCoCrCu0.5FeNi High Entropy Alloy (HEA) and High Entropy Ceramic (HEC) Thin Films," University of Sydney, University of Sydney, 2021.

[64] H. H. S. Gatzen, V.; Leuthold, J., "Micro and Nano Fabrication: Tools and Processes.," V. S. a. J. L. H. H. Gatzen Ed. Berlin, Heidelberg: Springer Berlin Heidelberg, 2015, pp. 65-203.

[65] M. P. S. a. F. Center. "What is Plasma?" https://www.psfc.mit.edu/vision/what_is_plasma (accessed Feb 01, 2022).

[66] F. F. Chen, *Introduction to Plasma Physics and Controlled Fusion*. New York, 1984.

[67] G. A. Mesyats, *Explosive Electron Emission*. Ekaterinburg: URO Press, 1998.

[68] G. A. Mesyats, *Cathode Phenomena in a Vacuum Discharge: The Breakdown, the Spark, and the Arc*. Moscow, Russia: Nauka, 2000.

[69] J. Prock, *Journal of Physics D: Applied Physics,* vol. 19, p. 1917, 2000.

[70] J. E. Daalder, "Random walk of cathode spots: a random walk of definitions? Reply by J E Daalder," *Journal of Physics D: Applied Physics,* vol. 16, no. 9, p. L177, 1983/09/14 1983, doi: 10.1088/0022-3727/16/9/303.

[71] D. M. Sanders and A. Anders, "Review of cathodic arc deposition technology at the start of the new millennium," *Surface and Coatings Technology,* vol. 133-134, pp. 78-90, 2000/11/01/ 2000, doi: https://doi.org/10.1016/S0257-8972(00)00879-3.

[72] I. G. Brown, *Annual Review of Materials Science,* vol. 28, 243-269, 1998.

[73] A. Anders, *Vacuum Technology & Coating*. 2002.

[74] S. Uhlmann, T. Frauenheim, and Y. Lifshitz, "Molecular-Dynamics Study of the Fundamental Processes Involved in Subplantation of Diamondlike Carbon," *Physical Review Letters,* vol. 81, no. 3, pp. 641-644, 07/20/ 1998, doi: 10.1103/PhysRevLett.81.641.

[75] Y. Lifshitz, S. R. Kasi, J. W. Rabalais, and W. Eckstein, "Subplantation model for film growth from hyperthermal species," (in eng), *Phys Rev B Condens Matter,* vol. 41, no. 15, pp. 10468-10480, May 15 1990, doi: 10.1103/physrevb.41.10468.

[76] C. Ronning, "Ion-beam synthesis and growth mechanism of diamond-like materials," *Applied Physics A,* vol. 77, no. 1, pp. 39-50, 2003/06/01 2003, doi: 10.1007/s00339-002-2063-7.

[77] R. L. G. I. I. B. Beilis, S.; Paperny, V.L., , "Radially expanding plasma parameters in a hot refractory anode vacuum arc," *J. Appl. Phys,* vol. 88, p. 3036, 2000.

[78] M. Enomoto, "The N-Ti-V system (nitrogen-titanium-vanadium)," *Journal of Phase Equilibria,* vol. 17, no. 3, pp. 248-252, 1996/06/01 1996, doi: 10.1007/BF02648494.

[79] F. Tessier *et al.*, "Energetics of binary iron nitrides," *Solid State Sciences,* vol. 2, no. 4, pp. 457-462, 2000/06/04/ 2000, doi: https://doi.org/10.1016/S1293-2558(00)00151-5.

[80] R. C. Weast, in *CRC Handbook of Chemistry and Physics*, vol. C528-C529, R. C. Weast Ed., 51st edition ed. Cleveland, OH: Chemical Rubber Co., 1971.

[81] G. H. Aylward, *SI chemical data / Gordon Aylward & Tristan Findlay* (no. Accessed from https://nla.gov.au/nla.cat-vn21060). Milton, Qld: John Wiley & Sons, 2002.

[82] J. Patscheider, "Nanocomposite Hard Coatings for Wear Protection," *MRS Bulletin,* vol. 28, no. 3, pp. 180-183, 2003, doi: 10.1557/mrs2003.59.

[83] I. A. Abrikosov *et al.*, "Phase Stability and Elasticity of TiAlN," *Materials*, vol.

4, no. 9, pp. 1599-1618doi: 10.3390/ma4091599.

[84] U. Jansson and E. Lewin, "Sputter deposition of transition-metal carbide films — A critical review from a chemical perspective," *Thin Solid Films,* vol. 536, pp. 1–24, 06/01 2013, doi: 10.1016/j.tsf.2013.02.019.

[85] R. T. Balmer, in *Modern Engineering Thermodynamics*, R. T. Balmer Ed.: Academic Press, 2011, pp. 727-762.

[86] S. Mahieu *et al.*, "Biaxially aligned titanium nitride thin films deposited by reactive unbalanced magnetron sputtering," *Surface and Coatings Technology,* vol. 200, no. 8, pp. 2764-2768, 2006/01/24/ 2006, doi: https://doi.org/10.1016/j.surfcoat.2004.09.012.

[87] C.-H. Lai, S.-J. Lin, J.-W. Yeh, and S.-Y. Chang, "Preparation and characterization of AlCrTaTiZr multi-element nitride coatings," *Surface and Coatings Technology,* vol. 201, no. 6, pp. 3275-3280, 2006/12/04/ 2006, doi: https://doi.org/10.1016/j.surfcoat.2006.06.048.

[88] S. Sasmal and M. B. Anoop, "7 - Nanoindentation for evaluation of properties of cement hydration products," in *Nanotechnology in Eco-efficient Construction (Second Edition)*, F. Pacheco-Torgal, M. V. Diamanti, A. Nazari, C. G. Granqvist, A. Pruna, and S. Amirkhanian Eds.: Woodhead Publishing, 2019, pp. 141-161.

[89] M. Bilek, P. Martin, and D. McKenzie, "Influence of gas pressure and cathode composition on ion energy distributions in filtered cathodic vacuum arcs," *Journal of Applied Physics,* vol. 83, pp. 2965-2970, 03/15 1998, doi: 10.1063/1.367052.

[90] H. Cao *et al.*, "Effect of nitrogen pressure on the microstructure, mechanical and electrochemical properties of CrAlN coatings deposited by filter cathode vacuum arc," *Ceramics International,* vol. 48, no. 24, pp. 36570-36584, 2022/12/15/ 2022, doi: https://doi.org/10.1016/j.ceramint.2022.08.216.

[91] Britannica. "Mean Free Path." Encyclopedia Britannica. https://www.britannica.com/science/mean-free-path (accessed July 07, 2023).

[92] M. F. S. Roger Kelly, *Materials Modification by High-fluence Ion Beams* (NATO Science Series E). 1989.

[93] H. Zhao *et al.*, "High entropy alloy thin films on SS304 substrates: Evolution of microstructure and interface modulated by energetic condensation in nanoscale," *Materials & Design,* vol. 230, p. 111981, 2023/06/01/ 2023, doi: https://doi.org/10.1016/j.matdes.2023.111981.

[94] A. Anders, "Film Deposition by Energetic Condensation," in *Cathodic Arcs: From Fractal Spots to Energetic Condensation*, A. Anders Ed. New York, NY: Springer New York, 2008, pp. 363-407.

[95] S. H. Elder, F. J. DiSalvo, L. Topor, and A. Navrotsky, "Thermodynamics of ternary nitride formation by ammonolysis: application to lithium molybdenum nitride (LiMoN2), sodium tungsten nitride (Na3WN3), and sodium tungsten oxide nitride (Na3WO3N)," *Chemistry of Materials,* vol. 5, no. 10, pp. 1545-1553, 1993/10/01 1993, doi: 10.1021/cm00034a027.

[96] M. W. Chase, Jr., "NIST-JANAF Thermochemical Tables, Fourth Edition," *J. Phys. Chem. Ref. Data,* vol. Monograph 9, pp. 1-1951, 1998.

[97] "CRC Handbook of Chemistry and Physics: A Ready-Reference of Chemical and Physical Data, 85th ed Edited by David R. Lide (National Institute of Standards and Technology). CRC Press LLC: Boca Raton, FL. 2004. 2712 pp. $139.99. ISBN 0-8493-0485-7," *Journal of the American Chemical Society,* vol. 127, no. 12, pp. 4542-4542, 2005/03/01 2005, doi: 10.1021/ja041017a.

[98] C.-Y. Yeh, Z. W. Lu, S. Froyen, and A. Zunger, "Zinc-blende--wurtzite polytypism in semiconductors," *Physical Review B,* vol. 46, no. 16, pp. 10086-10097, 10/15/ 1992, doi: https://doi.org/10.1103/PhysRevB.46.10086.

[99] I.-k. Suh, H. Ohta, and Y. Waseda, "High-temperature thermal expansion of six metallic elements measured by dilatation method and X-ray diffraction Locality: synthetic Sample: at T = 293 K," 1988, doi: https://doi.org/10.1007/BF01174717.

[100] Z. S. Basinski, W. Hume-Rothery, and A. L. Sutton, "The Lattice Expansion of Iron," *Proceedings of the Royal Society of London. Series A, Mathematical and Physical Sciences,* vol. 229, no. 1179, pp. 459-467, 1955. [Online]. Available: http://www.jstor.org/stable/99693.

[101] L. Marick, "Variation of Resistance and Structure of Cobalt with Temperature and a Discussion of Its Photoelectric Emission," *Physical Review,* vol. 49, no. 11, pp. 831-837, 06/01/ 1936, doi: 10.1103/PhysRev.49.831.

[102] W. D. Callister Jr., *Fundamentals of Materials Science and Engineering: An Integrated Approach, Enhanced eText*, 5th ed. Wiley, 2018.

[103] A. Anders, "A structure zone diagram including plasma-based deposition and ion etching," *Thin Solid Films,* vol. 518, pp. 4087-4090, 05/01 2010, doi: 10.1016/j.tsf.2009.10.145.

[104] H. Cao *et al.*, "Effect of nitrogen pressure on the microstructure, mechanical and electrochemical properties of CrAlN coatings deposited by filter cathode vacuum arc," *Ceramics International,* 2022/08/27/ 2022, doi: https://doi.org/10.1016/j.ceramint.2022.08.216.

[105] N. C. f. B. Information. "Atomic Radius in the Periodic Table of Elements." https://pubchem.ncbi.nlm.nih.gov/periodic-table/atomic-radius (accessed Jul 02, 2023).

[106] K. von Fieandt, L. Riekehr, B. Osinger, S. Fritze, and E. Lewin, "Influence of N content on structure and mechanical properties of multi-component Al-Cr-Nb-Y-Zr based thin films by reactive magnetron sputtering," *Surface and Coatings Technology,* vol. 389, p. 125614, 2020/05/15/ 2020, doi: https://doi.org/10.1016/j.surfcoat.2020.125614.

[107] Q. Wan *et al.*, "Microstructure and mechanical properties of FeCoCrNiAl0.1N high entropy alloy nitride coatings synthesized by cathodic arc ion plating using alloy target," *Surface and Coatings Technology,* vol. 457, p. 129305, 2023/03/25/ 2023, doi: https://doi.org/10.1016/j.surfcoat.2023.129305.

[108] S.-S. Zhao *et al.*, "Deposition of thick TiAlN coatings on 2024 Al/SiCp substrate

by Arc ion plating," *Surface and Coatings Technology,* vol. 202, no. 21, pp. 5170-5174, 2008/07/30/ 2008, doi: https://doi.org/10.1016/j.surfcoat.2008.05.041.

[109] Z. Zheng *et al.*, "Enhanced strength of AlCoCrCu0.5FeNi high entropy alloy thin films reinforced by multi-phase hardening and nanotwins," *Materials Science and Engineering: A,* vol. 879, p. 145252, 2023/07/10/ 2023, doi: https://doi.org/10.1016/j.msea.2023.145252.

[110] Z. Zheng, H. Zhao, L. Sun, M. M. Bilek, and Z. Liu, "The microstructural evolution of dual phase high entropy alloy thin films by annealing," *Journal of Alloys and Compounds,* vol. 953, p. 170102, 2023/08/25/ 2023, doi: https://doi.org/10.1016/j.jallcom.2023.170102.

[111] G. J. Gao, J. L. Xu, J. Tang, L. W. Zhang, Y. C. Ma, and J. M. Luo, "Plasma nitrided CoCrFeNiMn high entropy alloy coating as a self-supporting electrode for oxygen evolution reaction," *Journal of Materials Research and Technology,* vol. 23, pp. 5357-5367, 2023/03/01/ 2023, doi: https://doi.org/10.1016/j.jmrt.2023.02.135.

[112] Z.-C. Chang, S.-C. Liang, S. Han, Y.-K. Chen, and F.-S. Shieu, "Characteristics of TiVCrAlZr multi-element nitride films prepared by reactive sputtering," *Nuclear Instruments and Methods in Physics Research Section B: Beam Interactions with Materials and Atoms,* vol. 268, no. 16, pp. 2504-2509, 2010/08/15/ 2010, doi: https://doi.org/10.1016/j.nimb.2010.05.039.

[113] R. Chen *et al.*, "Effects of nitriding on the microstructure and properties of VAlTiCrMo high-entropy alloy coatings by sputtering technique," *Journal of Alloys and Compounds,* vol. 827, p. 153836, 2020/06/25/ 2020, doi: https://doi.org/10.1016/j.jallcom.2020.153836.

[114] B. Ren, Z. Shen, and Z. Liu, "Structure and mechanical properties of multi-element (AlCrMnMoNiZr)Nx coatings by reactive magnetron sputtering," *Journal of Alloys and Compounds,* vol. 560, pp. 171-176, 2013/05/25/ 2013, doi: https://doi.org/10.1016/j.jallcom.2013.01.148.

[115] B. Bhushan, *Principles and Applications of Tribology*. New York: A Wiley-Interscience Publication, 1999.

[116] P. K. Parsi. "Wear." https://www.tribonet.org/wiki/wear/ (accessed July 08, 2023).

[117] Z. H. Mohd Shadab Khan, Yaqoob Ali Ansari, *Friction and Wear of Materials*. New York, 1995.

[118] K. Kato, "Abrasive wear of metals," *Tribology International,* vol. 30, no. 5, pp. 333-338, 1997/05/01/ 1997, doi: https://doi.org/10.1016/S0301-679X(96)00063-1.

[119] H. Dong, "3 - Tribological properties of titanium-based alloys," in *Surface Engineering of Light Alloys*, H. Dong Ed.: Woodhead Publishing, 2010, pp. 58-80.

[120] M. R. Mahadeshwara. "Fretting Wear." https://www.tribonet.org/wiki/fretting-wear/ (accessed July 09, 2023).

[121] M. Roy, "6 - Tribological degradation at elevated temperature," in *Developments in High Temperature Corrosion and Protection of Materials*, W. Gao and Z. Li Eds.: Woodhead Publishing, 2008, pp. 117-163.

[122] G. W. S. a. A. W. Batchelor, *Engineering Tribology*, Fourth ed. 2014.

[123] H. M. Alojali and K. Y. Benyounis, "Advances in Tool wear in Turning Process," in *Reference Module in Materials Science and Materials Engineering*: Elsevier, 2016.

[124] M. R. Mahadeshwara. "Corrosive Wear." https://www.tribonet.org/wiki/corrosive-wear/#:~:text=Definition%3A,agents%2C%20lubricants%20or%20atmospheric%20mediums. (accessed July, 2023).

[125] J.-J. Wang, S.-Y. Chang, and F.-Y. Ouyang, "Effect of substrate bias on the microstructure and properties of (AlCrSiNbZr)Nx high entropy nitride thin film," *Surface and Coatings Technology,* vol. 393, p. 125796, 2020/07/15/ 2020, doi: https://doi.org/10.1016/j.surfcoat.2020.125796.

[126] Y.-C. Lin *et al.*, "Improving the hardness of high entropy nitride (Cr0.35Al0.25Nb0.12Si0.08V0.20)N coatings via tuning substrate temperature and bias for anti-wear applications," *Surface and Coatings Technology,* vol. 403, p. 126417, 2020/12/15/ 2020, doi: https://doi.org/10.1016/j.surfcoat.2020.126417.

[127] A. V. Pshyk *et al.*, "High-entropy transition metal nitride thin films alloyed with Al: Microstructure, phase composition and mechanical properties," *Materials & Design,* vol. 219, p. 110798, 2022/07/01/ 2022, doi: https://doi.org/10.1016/j.matdes.2022.110798.

Supplementary Information

Cathodic arc deposition information

Figure S1 illustrates the structure of the filtered cathodic arc deposition system used in this project. Nitrogen was introduced near the substrate side of the filter chamber.

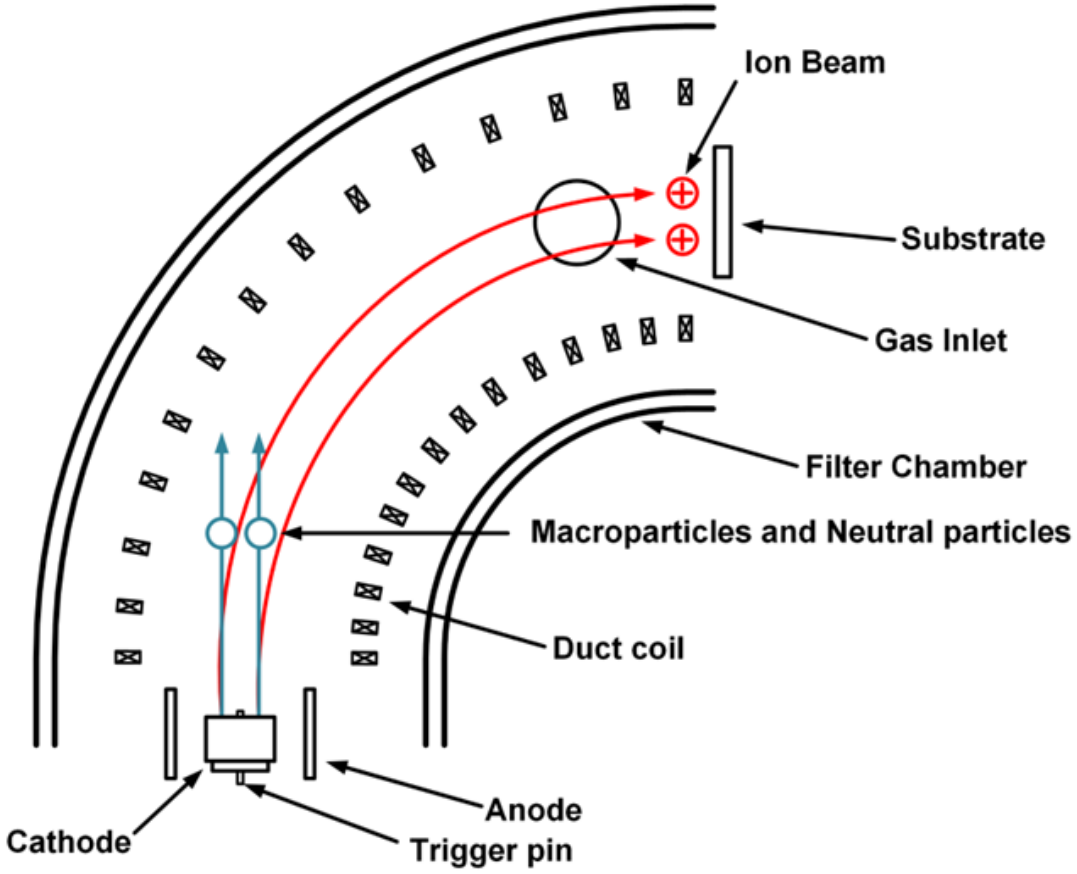

Figure S1. Cathodic arc deposition system with a half-semicircle filter chamber, gas inlet near the substrate

Profilometer supplementary information

Figure S2 illustrates the valley created by a physical mask placed on the substrate when depositing $AlCrFeCoNiCu_{0.5}$ HEA and HEN thin films at various pressure. Physical masking was formed by scribing with acetone-soluble markers, with each line no less than 1mm thick and 0.5 mm wide. Each thin film was cleaned at least three times for 5 minutes in an ultrasonic solution of acetone, ethanol and deionised water after

deposition to remove the physical mask, creating a valley. The height difference measured by the Dektak profilometer represented the thickness of each thin film at the scanning point. To prevent damage to the pin equipped in the profilometer and ensure measurement accuracy, the scanning direction is set from the thin film surface (higher surface) to the substrate (lower surface).

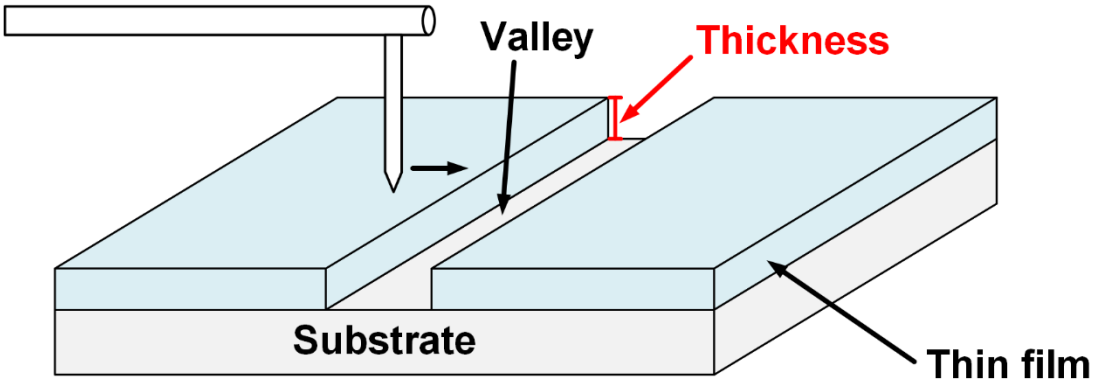

Figure S2. A schematic diagram shows an example of a valley created for thin film deposition and how the thickness is measured.

XPS spectra supplementary information

X-ray photoelectron spectroscopy (XPS) was utilised to investigate the surface chemistry of each thin film. The impact nitrogen pressure had on the surface chemistry of the films was also explored. As shown in Figure S3, the XPS survey spectra reveal the signals of each element in the thin films. Nitrogen signal only exhibited in the HEN thin films deposited at 0.01 Pa and 0.05 Pa, corresponding to the findings in EDS.

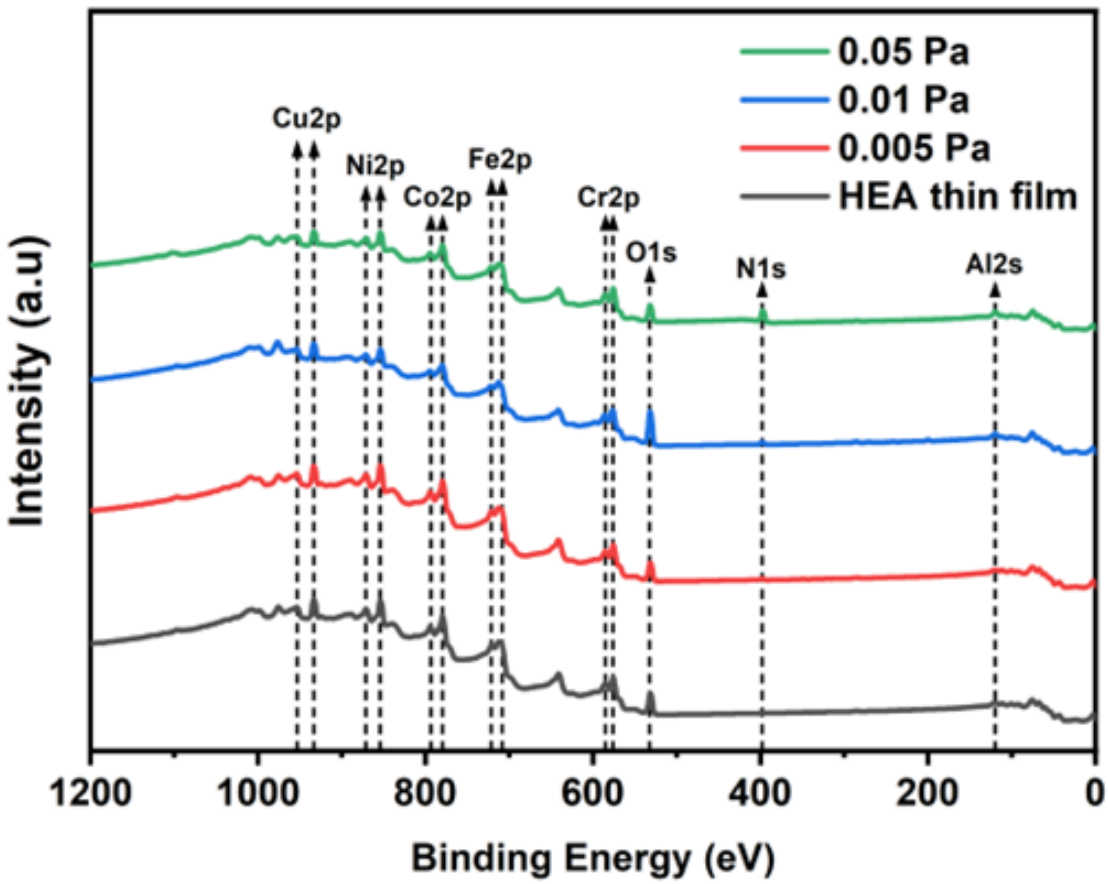

Figure S3. XPS survey spectra for each $AlCrFeCoNiCu_{0.5}$ HEA and HEN thin film deposited at various pressures.

XRD supplementary information

The XRD pattern ranged from 20° to 90° is shown in Figure S4. A prominent Si (400) peak in the XRD pattern, attributed to the Si wafer, obscures the visibility of smaller peaks. To clearly show the evolution of crystallinity in the thin film, the XRD pattern with a range of 30° to 60° of 2θ angle was selected. The unknown peak indexed at 47.8° was observed in all XRD patterns of the substrate and thin films, indicating that this peak was attributed to the Si wafer.

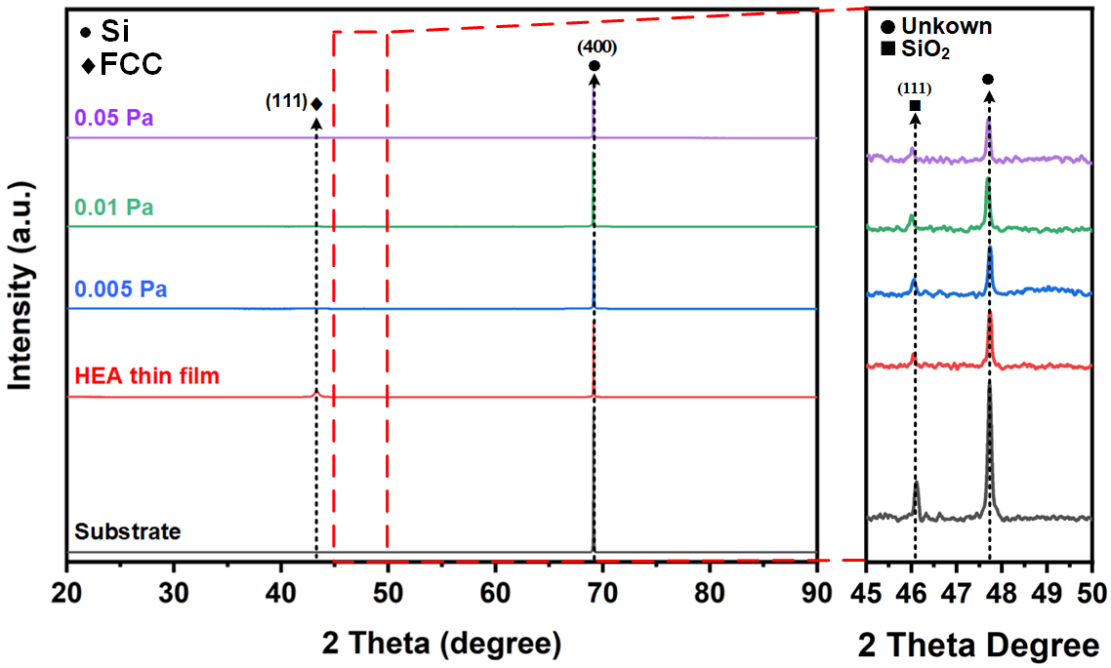

Figure S4. XRD pattern range from 20° to 90° of Si wafer substrate and each $AlCrFeCoNiCu_{0.5}$ HEA and HEN thin film deposited at various pressures.